IMPACT FORCE AND MOMENT PROBLEMS ON RANDOM FIELDS WITH
FRACTAL AND HURST EFFECTS

BY

XIAN ZHANG

DISSERTATION

Submitted in partial fulfillment of the requirements
for the degree of Doctor of Philosophy in Theoretical and Applied Mechanics
in the Graduate College of the
University of Illinois Urbana-Champaign, 2021

Urbana, Illinois

Doctoral Committee:

Professor Martin Ostoja-Starzewski, Chair
Professor Paul Fischer
Assistant Professor Kathryn Matlack
Associate Professor Ahmed Ettaf Elbanna

Abstract

Wave propagation through random heterogeneous media is an important research area due to its significance in engineering and science applications. This dissertation focuses on the investigation of dynamical responses of Lamb's wave propagation through random media with fractal and Hurst effects. Inspired by nature, we use fractal and Hurst parameters to characterize the spatial randomness. Two random field models, namely, Cauchy and Dagum models, have been employed to model both mass density and stiffness tensor fields. Since there exists no closed solution for transient waves in random media, we adopt and generalize a numerical scheme called cellular automata (CA) to simulate the dynamical responses.

We first investigate cellular automata's response to an anti-plane, impulse line load on a half-space on random mass density random fields. In this study, we validate our numerical solver by comparing simulated responses on white noise with the homogeneous results and the theoretical, analytical solution from classical elasticity theory. Evaluation of stochastic imperfection sensitivity has shown that the shear wave is less sensitive to spatial fluctuations compared with pressure and Rayleigh waves. We then generalize the cellular automata to in-plane force and moment problems on random mass density fields. We find out that the responses are more sensitive to Hurst parameter than the fractal dimension for all loading scenarios. The sensitivity for all loading cases are also presented and compared with one another both qualitatively and quantitatively. To fully capture the complexity of material spatial randomness requires the consideration of both mass density and stiffness tensor. In the last part of this thesis, we adopt a novel second-rank anti-plane stiffness tensor random field (TRF) model by taking the dyadic product of two scalar random fields. This model

allows us to represent full anisotropy with heterogeneity. With the introduction of random mass density field, a comparion study for anti-plane Lamb's problem is conducted among three stiffness tensor models: (1) a deterministic stiffness tensor; (2) a locally isotropic stiffness tensor with heterogeneity; (3) a second-rank tensor admitting full anisotropy and heterogeneity. The simulation results show that the fluctuation of displacement reponses on model (3) is the strongest, followed by model (2), and then by model (1). in general, this thesis has made contributions in areas of random field modeling, numerical scheme for elastodynamics and sensitivity analysis for wave propagations.

To my family,

My mom: Ping Xie, for giving my life and everything that really matters in life.

My dad: Longyun Zhang, for nurturing my curiosity and love for math and science.

My grandmom: Wanmei Xu, for teaching me that it is all about survival.

Acknowledgments

I would firstly like to express gratitude to my advisor, Prof. Martin Ostoja-Starzewski. Thank you for your investment in my Ph.D. journey and constantly pushing me towards a higher level. I was able to explore many ideas while receiving continuous guidance and inspiration. I would also like to thank Dr. Vinesh Nishawala, whose encouragement helped me through many ups and downs of this journey. I find myself very fortunate to have him as a mentor and as a friend to share my research at UIUC. I am also grateful to two professors that I respect very much. Prof. Paul Fischer introduced me to computational mechanics through his finite element class. His passion in numerical research is a constant inspiration. Prof. Katie Matlack made insightful remarks that shed light on my research while I was trying to explore more ideas and attend one semester of her group meeting. It is my great fortune and honor to receive mentorship from these outstanding professors. I would like to Prof. Elbanna for his time and effects in reviewing my prelim and this Ph.D. thesis. The work in this thesis would not have been possible without the collaborative work from all the great colleagues that I have the pleasure to work with. I want to thank Dr. Dansong Zhang, Amirhossein Amiri-Hezaveh and Dr. Bharath Raghavan for their close collaborations that crystallized many inspiring ideas into fruitful results. I extend my gratitude to Dr. Taishan Zhu for his helpful advices, and special thanks to Dr. Ophelia Bolmin for her being an incredible role model during the last year and job hunting process during this special pandemic time. Thank you also to the MechSE staff and Professors, especially Kathy Smith, for guiding me through all of the necessary paperwork and requirements and teaching me how to think and how to enjoy research. Finally, I want to thank my friends that I met along the way, Keong, Lana, Oyuna, Mihary, Ben, Ophelia, and others. You have made this journey special. Most importantly, I want to thank my family for their unconditional love and support. My caring parents Ping Xie and Longyun Zhang, my nourishing grandparents, my loving husband Dr. Yanran Ding, who is always so resilient, supportive and is my ultimate inspiration.

Contents

---

[1]The content about random mass density fields presented here is mainly taken from our work in [64].

[2]The content about tensor random fields presented here is taken from Ostoja-Starzewski's work in [63].

List of Figures

List of Tables

Chapter 1

Introduction

1.1 Motivation

Classical wave propagation theory assumes deterministic and homogeneous material properties while spatial randomness including both inhomogeneity and anisotropy are found in many materials [35, 38]. This thesis aims to model the spatial randomness and simulate the dynamical displacement and stress responses on the modeled random media to address the question whether the effective medium wave equations can work for transient wave problems in random media. Several classical elastostatic and elastodynamic problems with homogeneous material properties have been formulated and studied extensively in classical elasticity: Kelvin, Cerruti, Boussinesq, Lamb, Mindlin [2, 40] over the last century. In this thesis work, we focus on anti-plane and in-plane Lamb-type elastodynamic problems and continue the investigations of displacement and stress responses on media with spatial randomness.

Recently, material models have evolved from purely deterministic to probabilistic to statistical models that incorporate the hybrid concept of regionalized variables [6, 30, 35]. Due to their importance in almost any scientific discipline, spatial random fields (SRF) constitute an active area of current research. The simplest way to model spatial randomness is to use white noise analysis, which has been developed extensively in recent years [14]. Most random fields are complex systems that are parameterized by some space-time parameters [10, 36, 42, 62]. Motivated by numerous natural media settings [27], the randomness in this study was assumed to have fractal and Hurst effects. Following a series of recent studies, we first investigated the anti-plane and in-plane Lamb problems in media with random

fields of mass density and spatially homogeneous isotropic linear elasticity [34, 64, 65]. In order to consider the overall spatial randomness, we then extend these studies to include such randomness also in the anti-plane stiffness tensor, while admitting its full anisotropy, i.e. not forcing it to be locally isotropic.

To model the scalar mass density RF, we work with second-order, wide-sense stationary and isotropic models with Cauchy or Dagum correlation functions [8, 11, 43]. Such random fields can capture and decouple fractal and Hurst effects and have been employed in the study of 1d spatial settings and random process loadings [32, 51, 52]. To model the spatial statistics of the anti-plane stiffness tensor with full anisotropy, we work with a second-rank tensor random field (TRF) [25, 26, 63]. This is done by taking the dyadic product of two scalar random fields generated from Cauchy or Dagum correlation functions.

Since there exists no closed solution for transient waves in the introduced random media, we resort to numerical investigations. A numerical scheme called cellular automata (CA) is adopted and developed to simulate the anti-plane responses for the following two reasons: (i) CA allows individual assignment of heterogeneous material properties for each cell and (ii) the rectangular-celled CA is mathematically equivalent to a central finite difference method which is analytically equivalent to the linear partial differential equations of classical elasticity.

Generally, the governing field equation of a deterministic mechanics system reads

$$\mathcal{L}\mathbf{u} = f, \tag{1.1}$$

where $\mathcal{L}$ is (usually) a differential operator, $\mathbf{u}$ is a displacement field, and f is an applied loading source. If we introduce randomness into the material properties (into both mass density and mechanical properties), then (1.1) is replaced by a stochastic field equation

incorporating the spatial fluctuation

$$\mathcal{L}(\omega)\mathbf{u} = f; \quad \omega \in \Omega. \tag{1.2}$$

Here ω is a single realization of the sample space Ω which together with a σ-algebra S and a probability measure P on it forms a probability space (Ω, S, P). Typically, a Gaussian measure is assumed, although, if more information about the material randomness is available, other types of probability distribution are possible. The space (Ω, S, P) defines a random medium $\mathcal{B} = \{B(\omega); \omega \in \Omega\}$.

The ensemble average (i.e., the stochastic expectation) of $\mathcal{L}$ is simply

$$\langle \mathcal{L} \rangle = \int_\Omega \mathcal{L}(\omega) dP, \tag{1.3}$$

and, as always for stochastic systems, one is first interested in the average displacement response $\langle \mathbf{u} \rangle$ before inquiring about the second and higher moments, and, ideally, about the probability distribution of the response. The above straightforward averaging of 1.3 leads to a deterministic field equation

$$\langle \mathcal{L} \rangle \mathbf{u}_{\text{det}} = f, \tag{1.4}$$

where $\mathbf{u}_{\text{det}}$ is the deterministic (and supposedly right...) solution. However, a correct solution of the stochastic problem 1.2 is formally obtained by first inverting 1.3, then averaging, and then inverting again:

$$\left\langle \mathcal{L}^{-1} \right\rangle^{-1} \langle \mathbf{u} \rangle = f. \tag{1.5}$$

In general, there is no closed-form solution to 1.5. So the basic question asked in stochastic mechanics is: if one replaces $\langle \mathcal{L}^{-1} \rangle^{-1}$ by $\langle \mathcal{L} \rangle$, how different will the solutions $\langle \mathbf{u} \rangle$ and $\mathbf{u}_{\text{det}}$ be?

Once this is answered, the next task is to determine whether the noise-to-signal ratio of the

random response

$$CV_R := \frac{SD_R}{mean_R}. \tag{1.6}$$

is stronger (or weaker) than the noise-to-signal ratio of the underlying RF (describing the random medium $\mathcal{B} = \{B(\omega); \omega \in \Omega\}$)

$$CV_{RF} := \frac{SD_{RF}}{mean_{RF}}. \tag{1.7}$$

Here SD and CV stand for the standard deviation and the coefficient of variation of some chosen random property, respectively. In the situations where the mean is close or equal to zero, CV loses its meaning and then the signal-to-noise ratios have to be employed

$$SNR_R := \frac{1}{CV_R} = \frac{mean_R}{SD_R}, \tag{1.8}$$

$$SNR_{RF} := \frac{1}{CV_{RF}} = \frac{mean_{RF}}{SD_{RF}}. \tag{1.9}$$

The scope of this thesis is limited to a numerical study of force and moment problems of Lamb's wave propagation on random media with fractal and Hurst effects. Investigations of static responses of an elastic half-plane with random boundary conditions, albeit without the fractal and Hurst effects can be found in [47, 48]. One can also find many theoretical, analytical studies focusing on diffusion type problems in random media in the literature, o, e.g. [12, 13, 15].

1.2 Related work

The area of stochastic wave propagation has progressed rapidly thanks to the enormous amount of research on random field modeling and numerical modeling for elastodynamics. A rough categorization of the related work in these areas is presented in this section. Random fields with fractal and Hurst effects for both mass density field and tensor field were

introduced. Detailed visualizations for scalar random fields and tensor random fields can be found in Chapter 2 and Chapter 4 respectively. The overall framework for cellular automata is also introduced here although the detailed updating equations and stepping algorithms can be found in each elastic half-plane problem.

1.2.1 Random mass density fields [1]

Te introduce the randomness into the mass density field, we introduce a mass density RF over the 2d domain $X \in \mathbb{R}^2$:

$$\rho\left(\omega, \mathbf{x}\right) : \Omega \times X \to \mathbb{R}; \quad \omega \in \Omega, \quad \mathbf{x} \in X, \tag{1.10}$$

where $\mathbf{x}$ is location in the plane and ω is a single event of the sample space Ω which together with a σ-algebra S and a probability measure P on it forms a probability space (Ω, S, P). Typically, a Gaussian measure is assumed, although, if more information about the material randomness is available, a transformation to other types of probability distribution is possible. The space (Ω, S, P) defines a random medium $\mathcal{B} = \{B(\omega); \omega \in \Omega\}$. Since many conspicuous patterns in nature can be imitated by fractal geometry [27,28] and Hurst characteristics, two stochastic models which can capture fractal behavior and Hurst effects have been devlopled: Cauchy and Dagum [11,41,43]. In general, the fractal dimension denoted by D can be described as a roughness measure that ranges from n to n + 1 for a n-dimensional system. Typically, the larger is the fractal dimension, the rougher are the field's realizations. The Hurst parameter denoted by H describes the long-range dependence. In general, an anti-persistent system is associated with $H \in \left(0, 0.5\right)$ while a persistent system has $H \in \left(0.5, 1\right)$. For $H = 0.5$, the system reflects a true random walk without any long-range dependence.

The explicit forms (except for the simplest Cauchy case where $\alpha = 2$) of spectral densities

---

[1]The content about random mass density fields presented here is mainly taken from our work in [64].

are rather complicated, so analytically solving initial-boundary value problems of 2d and 3d elastodynamics is generally hopeless. Explicit solutions are, to some extent, possible for simple 1d elastostatic problems [51, 52] and 1d linear dynamical systems [53, 54]. Since we focus on waves in 2d, we must run Monte Carlo simulations on a number of RFs to assess the averaged responses.

Random fields in Euclidean space $\mathbb{R}^n$, where our problems are set, are defined by their covariance function, $C : \mathbb{R} \times \mathbb{R} \to \mathbb{R}$:

$$C\left(\mathbf{x}_1, \mathbf{x}_2\right) = \langle Z\left(\mathbf{x}_1\right) Z\left(\mathbf{x}_2\right) \rangle - \langle Z\left(\mathbf{x}_1\right) \rangle \langle Z\left(\mathbf{x}_2\right) \rangle, \quad \mathbf{x}_1, \mathbf{x}_2 \in \mathbb{R}^n. \tag{1.11}$$

where $Z(x_1)$ and $Z(x_2)$ are random variables. The covariance function, $C\left(\mathbf{x}_1, \mathbf{x}_2\right)$, measures the strength of linear correlation between the two random variables, $Z(x_1)$ and $Z(x_2)$. If the random variables are uncorrelated then $C\left(\mathbf{x}_1, \mathbf{x}_2\right) = 0$.

Here, we consider RFs which are isotropic and wide-sense-stationary (WSS). The WSS assumption restricts the mean to be constant and the auto-correlation function, and consequently the covariance function, to be independent of shifts in $\mathbb{R}^n$, so the a mapping $\tilde{C} : \mathbb{R}^n \to \mathbb{R}$ exists such that

$$C\left(\mathbf{x}_1, \mathbf{x}_2\right) = \tilde{C}\left(\mathbf{x}_1 - \mathbf{x}_2\right), \quad \mathbf{x}_1, \mathbf{x}_2 \in \mathbb{R}^n. \tag{1.12}$$

The isotropic assumption restricts the autocovariance function to be independent of rotations, so that there exists a function $C_Z : [0, \infty) \to \mathbb{R}$ such that:

$$\tilde{C}\left(\mathbf{x}_1 - \mathbf{x}_2\right) = C_Z(r), \quad r \geq 0. \tag{1.13}$$

We define r $= ||x_1 - x_2||$, then for a white noise or uncorrelated RF, the covariace function is

$$C_{WN}(r) = \delta(r), \quad r \geq 0, \tag{1.14}$$

Table 1.1: Correlation length for the **Cauchy** RFs.

	$\beta = 0.2$	$\beta = 1.0$	$\beta = 1.2$	$\beta = 1.5$	$\beta = 1.8$
$\alpha = 0.2$	∞	∞	1	0.09	0.02
$\alpha = 0.5$	∞	∞	3.57	1	0.48
$\alpha = 0.8$	∞	∞	4.63	1.70	1
$\alpha = 1.0$	∞	∞	5	2	1.25
$\alpha = 1.2$	∞	∞	5.23	2.21	1.44
$\alpha = 1.5$	∞	∞	5.46	2.42	1.64
$\alpha = 1.8$	∞	∞	5.60	2.56	1.77

where δ is the Dirac delta function.

The covariance function for a Cauchy RF is

$$C_C(r) = (1 + r^\alpha)^{-\frac{\beta}{\alpha}}, \quad r \geq 0, \ \alpha \in (0, 2], \ \beta > 0. \tag{1.15}$$

The covariance function for a Dagum RF is

$$C_D(r) = 1 - (1 + r^{-\beta})^{-\frac{\alpha}{\beta}}, \quad r \geq 0, \ \alpha \in (0, 1), \ \beta \in (0, 1]. \tag{1.16}$$

Both Cauchy and Dagum RFs models are capable of coupling and decoupling an arbitrary combination of fractial dimension D and Hurst coefficient H. The relationships between (D, H) and (n, α, β) in the above covariance functions are given by [31]

$$D = n + 1 - \frac{\alpha}{2}, \quad \text{and} \quad H = 1 - \frac{\beta}{2}, \tag{1.17}$$

where for two-dimensional systems, $n = 2$. Any combinations of α and β for both Cachy and Dagum RFs are generated using the RF package of R [49].

Typically, we use the correlation length of a RF as a characteristic length of the system, which is defined as

$$l = \int_0^\infty C(r) \mathrm{d}r. \tag{1.18}$$

Table 1.2: Correlation length for the **Dagum** RFs.

	$\beta = 0.2$	$\beta = 0.5$	$\beta = 0.8$
$\alpha = 0.2$	∞	∞	∞
$\alpha = 0.5$	∞	∞	∞
$\alpha = 0.8$	∞	∞	∞

The correlation length for Cauchy and Dagum RFs for several pairs of α and β are provided in Table 1.1 and 1.2 respectively. Introducing the scalar mass density field will be our first step to incorporate spatial randomness into the dynamic responses for Lamb's wave propagation problems.

1.2.2 Tensor random fields[2]

To fully capture the complexity of material spatial randomness requires the consideration of both mass density and stiffness tensor. Over the past years, some novel vector-valued and tensor-valued random field models have been developed using experimental data and upscaling techniques [4,50,55]. Recently, Ostoja-Starzewski *et al.* [63] has proposed to a way to construct a second-rank tensor that can both consider the inhomogeneity and anisotropy by taking the dyadic product of two scalar random fields. For this study, we adopt this anisotropic model and numerically simulate dynamic responses on the introduced random media. In this section, we introduce concepts associated with tensor random fields.

Assuming a linear elastic response throughout the entire material domain, the anti-plane shear response is described by a TRF of a rank-2 tensor:

$$\boldsymbol{C}\left(\omega, \mathbf{x}\right) : \Omega \times X \to \mathsf{S}^2\left(\mathbb{R}^2\right); \quad \omega \in \Omega, \quad \mathbf{x} \in X, \tag{1.19}$$

where $\mathsf{S}^2\left(\mathbb{R}^2\right)$ is the space of symmetric matrices. The field equation is a stochastic partial differential equation (SPDE) of anti-plane elastodynamics with local anisotropy (written in

---

[2]The content about tensor random fields presented here is taken from Ostoja-Starzewski's work in [63].

index notation)

$$[(C_{ij}u_{,j})]_{,i} = \rho\ddot{u}, \quad i,j = 1,2, \tag{1.20}$$

When $\boldsymbol{C} = C\boldsymbol{I}$ tends to C, the TRF in (1.19) becomes a random scalar field, whereupon (1.20) simplifies to a stochastic generalization of the anti-plane Navier equation of elastodynamics. This model accounts for the inhomogeneity while still assuming local isotropy. Now, micromechanics indicates that anisotropy must be present in spatially inhomogeneous random media. To account for it, the rank-2 symmetric TRF is modeled as a superposition of the isotropic mean with a dyadic. The latter is taken not in a general form of a product of two different random vectors, but as the simplest case: a product of the random vector $\mathbf{d} = d_1\mathbf{e}_1 + d_2\mathbf{e}_2$ with itself:

$$
\begin{aligned}
C_{ij} &= \left\langle C_{ij} \right\rangle + sC'_{ij}, \quad \left\langle C_{ij} \right\rangle = \mu\delta_{ij}, \\
C'_{ij} &= d_id_j, \quad \left[C'_{ij}\right] = \begin{bmatrix} d_1^2 & d_1d_2 \\ d_2d_1 & d_2^2 \end{bmatrix}.
\end{aligned}
\tag{1.21}
$$

Here each d_i $(i = 1,2)$ is $N(\mu_d, \sigma_d^2) = N(0,1)$ and independent from each other. s is a coefficient set so as to ensure that the tensor $\boldsymbol{C}$ is positive-definite.

A useful result: when a pair (X,Y) involves two normal random variables with mean zero, standard deviation 1, and no correlation ($\rho = 0$), then the pdf of the product $Z = XY$ is

$$
h_Z(z) = \begin{cases} K_0(-z)/\pi & -\infty < z < 0, \\ K_0(z)/\pi & 0 < z < \infty, \end{cases}
\tag{1.22}
$$

where K_0 is the modified Bessel function of second type and order zero. This pdf is not defined at 0.

The mean and variance of $C'_{11} = d_1^2 \ (= C'_{22})$ are

$$\langle C'_{11} \rangle = \sigma_d^2 = 1;$$
$$\sigma_{C_{11}}^2 \equiv Var\left(C_{(1)}\right) = \left\langle d_1^{2 \cdot 2} \right\rangle = 3\sigma_d^4 = 3,$$

(1.23)

with the pdf given by (1.22). The mean and variance of $C'_{12} = d_1 d_2 \ (= C'_{21})$ are

$$\langle C'_{12} \rangle = 0; \quad \sigma_{C_{12}}^2 \equiv Var\left(C_{12}\right) = \sigma_d^2 \sigma_d^2 = 3,$$

(1.24)

with the pdf given by (1.22).

The two basic invariants of C'_{ij} are

$$C'_{(1)} = C'_{ii} = d_1^2 + d_2^2,$$
$$C'_{(2)} = C'^2_{11} + 2C'_{12}C'_{12} + C'^2_{22}$$
$$= \left(d_1^2\right)^2 + 2\left(d_1 d_2\right)^2 + \left(d_2^2\right)^2.$$

(1.25)

The mean and variance of $C'_{(1)}$ are

$$\left\langle C'_{(1)} \right\rangle = \langle d_1^2 + d_2^2 \rangle = 2\sigma_d^2 = 2;$$
$$\sigma_{C_{(1)}}^2 \equiv Var\left(C_{(1)}\right) = \left\langle (d_1^2 + d_2^2)^2 \right\rangle = 2\left\langle d_1^4 \right\rangle = 6\sigma_d^4$$

(1.26)

The mean and variance of $C'_{(2)}$ are

10

$$\left\langle C'_{(2)} \right\rangle = \left\langle \left(d_1^2\right)^2 + 2\left(d_1 d_2\right)^2 + \left(d_2^2\right)^2 \right\rangle$$

$$= 4\left\langle d_1^4 \right\rangle = 4\sigma_d^2 = 4,$$

$$\sigma^2_{C'_{(2)}} \equiv Var\left(C'_{(2)}\right)$$

$$= \left\langle \left[\left(d_1^2\right)^2 + 2\left(d_1 d_2\right)^2 + \left(d_2^2\right)^2\right]^2 \right\rangle \qquad (1.27)$$

$$= \left\langle d_1^4 + 4d_1^3 d_2 + 6d_1^2 d_2^2 + 4d_1 d_2^3 + d_2{}^4 \right\rangle$$

$$= 2\left\langle d_1^4 \right\rangle + 8\left\langle d_1^3 d_2 \right\rangle + 6\left\langle d_1^2 d_2^2 \right\rangle$$

$$= 2\cdot 3\sigma_d^4 + 8\left\langle d_1^3 d_2 \right\rangle + 6\left\langle d_1^2 d_2^2 \right\rangle.$$

What can be said about the covariance of the entries C'_{ij}?

Some remarks are in order. Given two Cauchy correlations $\mathcal{C}_{\mu_i,\nu_i}$, with $i = 1, 2$, their product is again a correlation function. This is due to the fact that correlation functions are a convex cone that is closed under the topology of finite measures. Remarkably, the product $\widetilde{C}_{\mu_1,\mu_2,\nu_1,\nu_2} := \mathcal{C}_{\mu_1,\nu_1} \times \mathcal{C}_{\mu_1,\nu_1}$ does not belong to the generalized Cauchy family, except for the case $\widetilde{C}_{\mu_1,\mu_2,\nu} := \widetilde{C}_{\mu_1,\mu_2,\nu,\nu}$, which can be written as

$$\widetilde{C}_{\mu_1,\mu,\nu_1,\nu_2}(r) = \left(1 + r^{\mu_1+\mu_2}\right)^{-\nu} = \mathcal{C}_{\mu_1+\mu_2,\nu(\mu_1+\mu_2)}(r),$$

for $r \geq 0$. A second relevant remark is that for two given independent Gaussian random fields Z_i with covariance functions $\mathcal{C}_{\mu_i,\nu_i}$, with $i = 1, 2$, the random field $Y := Z_1 \times Z_2$ will have a covariance function $\widetilde{C}_{\mu_1,\mu_2,\nu_1,\nu_2}$. Yet, Y is not Gaussian, and hence its corresponding fractal dimension and Hurst effect cannot be calculated. For the sake of clarity, we call the class $\widetilde{C}_{\mu_1,\mu_2,\nu_1,\nu_2}$ the *MOSP Model* [63].

However, since the MOSP model is positive definite, there does exist a Gaussian random field, Y, having the MOSP model as covariance function. What can be said about its fractal and Hurst properties? We inquire about it for the case $\widetilde{C}_{\mu_1,\mu_2,\nu}$ as defined above. For investigation of the Hausdorff dimension of the graph, we look for a real number $\alpha \in (0, 2]$

11

such that

$$\lim_{r \to 0} \frac{\widetilde{C}_{\mu_1,\mu_2,\nu}(r) - 1}{r^\alpha} \tag{1.28}$$

is positive and finite. The function under the limit sign is

$$\frac{\widetilde{C}_{\mu_1,\mu_2,\nu}(r) - 1}{r^\alpha} = \frac{(1 + r^{\mu_1} + r^{\mu_2} + r^{\mu_1+\mu_2})^{-\nu} - 1}{r^\alpha} \tag{1.29}$$

Without loss of generality assume $\mu_1 \leq \mu_2$. If $\alpha = \mu_1$, we have by l'Hopital's rule

$$\begin{aligned}
\lim_{r \to 0} & \frac{1 - \widetilde{C}_{\mu_1,\mu_2,\nu}(r)}{r^\alpha} \\
&= \lim_{r \to 0}[\nu(1 + r^{\mu_1} + r^{\mu_2} + r^{\mu_1+\mu_2})^{-\nu-1}] \\
&\times \lim_{r \to 0} \frac{(\mu_1 r^{\mu_1-1} + \mu_2 r^{\mu_2-1} + (\mu_1 + \mu_2)r^{\mu_1+\mu_2-1})}{\mu_1 r^{\mu_1-1}}.
\end{aligned} \tag{1.30}$$

The first limit is ν, the second is 1 if $\mu_1 < \mu_2$ and 2 if $\mu_1 = \mu_2$. The Hausdorff dimension of the graph is $n + 1 - \min\{\mu_1, \mu_2\}/2$.

To investigate the Hurst effect, we look for a number $\beta \in (0, 1)$ such that

$$\lim_{r \to \infty} \frac{\widetilde{C}_{\mu_1,\mu_2,\nu}(r)}{r^{-\beta}} \tag{1.31}$$

is positive and finite. The case of $\beta = \nu(\mu_1 + \mu_2) \in (0, 1)$ solves the question. In this case, the random field under consideration has long memory, which can be characterized with Hurst coefficient

$$H = 1 - \frac{\nu(\mu_1 + \mu_2)}{2}. \tag{1.32}$$

We have not been able to derive further results for the general MOSP model $\widetilde{C}_{\mu_1,\mu_2,\nu_1,\nu_2}$, and this now stands as an open problem.

Explicit forms of the spectral density for the MOSP model are even more cumbersome. For given spectra associated with $\mathcal{C}_{\mu_i,\nu_i}$, $i = 1, 2$, the spectral density associated with the MOSP model would be the convolution of the original spectral densities associated with the

Generalized Cauchy model. This becomes an extremely challenging mathematical problem. To get the solutions of those stochastic partial differental equations and obtain the transient dynamic displacement and stress responses under scalar random fields and tensor random fields, we again resort to a numerical solver called celluar automata, which will be introduced in the next section.

1.2.3 Cellular automata

Cellular automata (CA) is a physics-based computational method, which was first proposed and implemented by John von Neumann [5, 58]. Cellular automata are among the simplest mathematical representations of complex systems and it has been widely adopted and extended as useful idealizations of the dynamic behavior of many real systems, including biological cellular networks [16], urban systems [3], neural networks [24], natual ecologies [46], among many others. The complex dynamic system behaviors, the characterizations of cellular automata and the different classes of CA algorithms can also be found in Wolfram's comprehensive review [59–61].

Recently, Leamy *et al.* [17, 20, 21] adapted this method to study the in-plane elastodynamics in a linear elastic medium. Their rectangular-celled CA is mathematically equivalent to a central finite difference method, although CA would require different stress assignment and boundary condition treatment. The state of each rectangular cell is dependent on the state of cells that share an edge or vertex with the cell. The cell's deformation and velocity, in both the x and y directions, are defined as the cell's state. In the framework of cellular automata, traction boundary conditions require an additional layer of cells assigned to the defined stress. Displacement boundary conditions are assigned directly. Through out this thesis, each chapter aims to detail the CA approach for corresponding forcing problem in terms of force, balance of momentum, stepping algorithm and boundary conditions.

1.3 Overview and contributions

This thesis contributes to the advancement of wave propagation in random media with more specific contributions including scalar random field modeling, numerical modeling for electrodynamics and tensor random field modeling to better describe material behaviors. The chapters in this thesis are organized in a progressive order, where anti-plane shear Lamb's problem on random mass density field is firstly investigated. Then follows a comprehensive study of in-plane Lamb's problem on random mass density field before we generalize the spatial randomness into anti-plane stiffness tensor. The sensitivity analysis is assessed for a wide range of fractal and Hurst effects for each proposed problem.

Chapter 2 starts with the simplest case: anti-plane shear Lamb's problem on random mass density fields with fractal and Hurst effects. We introduced two random fields models (Cauchy and Dagum) that are used to capture fractal dimension and Hurst effects in mass density field. A cellular automata (CA) framework is generalized and deployed to incorporate the spatial randomness, which will be our main numerical solver to simulate the shear wave propagation. The dynamic responses of random mass density are evaluated by comparing them with the homogeneous computational results and the classical solution. Then a comprehensive study is carried out for different combinations of fractal and Hurst coefficients. We study the spatial imperfection sensitivity and determine to what extent fractal and Hurst effects are significant enough to change the dynamic responses by comparing the the signal-to-noise ratio of the response versus the signal-to-noise ratio of the random field. This study also provides the general framework for more complicated forcing scenarios and random field modeling.

Chapter 3 continues our investigations in the setting of 2d RFs of mass density with fractal and Hurst effects. We presents an application of cellular automata (CA) to study the dynamic responses of Lamb-type problems for a continue our investigations in the setting of 2d RFs of mass density with such characteristics under a concentrated tangential point

load and a concentrated moment applied on the free surface of a half-plane. Given that there exist no adequate mathematical tools for transient waves in random-fractal media, we generalized the numerical, Monte Carlo-type cellular automata (CA) to simulate the in-plane elastodynamics. Sensitivity analysis for Pressure wave, Rayleigh wave and shear wave are separated and compared. Our study completes 2-D force and moment Lamb's problem under random mass density field by drawing comparisons to previously studied Lamb-type problems under a normal in-plane and anti-plane loading.

Chapter 4 introduces the same fractal and Hurst effects to a second-rank anti-plane stiffness tensor random field (TRF) model with full anisotropy. We then generalize the cellular automata solver to incorporate the spatial randomness both in mass density as well as the stiffness tensor fields. A comprehensive sensitivity comparion study for anti-plane Lamb's problem is conducted among three stiffness tensor models: (1) a deterministic stiffness tensor; (2) a locally isotropic stiffness tensor with heterogeneity; (3) a second-rank tensor admitting full anisotropy and heterogeneity. The simulation results show that the fluctuation of anti-plane shear wave reponses on model (3) is the strongest, followed by model (2).

Chapter 5 provides the concluding remarks and introduces the possible future research directions from this thesis.

Chapter 2

Anti-plane shear Lamb's problem on random mass density fields[1]

Let's start with the simplest case: anti-plane shear Lamb's problem on random mass density fields with fractal and Hurst effects. This chapter reports the dynamic responses of anti-plane shear Lamb's problem on random mass density field with fractal and Hurst effects. Cellular automata (CA) is used to simulate the shear wave propagation. Both Cauchy and Dagum random field models are used to capture fractal dimension and Hurst effects in mass density field. We first evaluate the dynamic responses of random mass density by comparing them with the homogenerous computational results and the classical theoretical solution. Then a comprehensive study is carried out for different combinations of fractal and Hurst coefficients. We study the spatial imperfection senstivity and determine to what extent fractal and Hurst effects are significant enough to change the dynamic responses by comparing the the signal-to-noise ratio of the response versus the signal-to-noise ratio of the random field [64].

The random mass density field ρ is defined over a probability space (Ω, S, P):

$$\rho(\omega, \mathbf{x}) : \Omega \times X \to \mathbb{R}^2; \quad \omega \in \Omega, \quad \mathbf{x} \in X, \tag{2.1}$$

where S denotes a σ-algebra, P represents a Gaussian measure and X indicates a two-dimensional domain of interest in $\mathbb{R}^2$.

Numerical investigations of SH-wave propagation in inhomogeneous and random media are intensive over the past decades. Manolis *et al.* [29] have developed Green's functions for SH

---

[1]The content of this chapter is mostly taken out from our work in [64].

waves in an elastic continuum exhibiting large randomness. Finite difference simulations are still among the most popular numerical solvers to obtain the dynamic displacement and stress responses [9, 57]. The SH wave motion involves the anti-plane displacement $u \equiv u_z(x, y, t)$ whose governing stochastic equation is

$$\nabla^2 u + f_z(x, y, t) = \rho(\omega, \mathbf{x}) \frac{\partial^2 u}{\partial t^2}; \quad \omega \in \Omega, \quad \mathbf{x} \in (x, y)\text{-plane}, \tag{2.2}$$

where t is the time, $\mathbf{x}$ is the coordinate in underformed configuration, and σ_{xz}, σ_{yz} are the shear stresses; the body force field is absent in our considerations. The classical approach in the stochastic wave propagation literature is to seek a solution for such a system in the frequency domain through a stochastic Helmholz equation [23]. However, since the Cauchy and Dagum RFs have no explicit spectral densities [19] (i.e., Fourier transforms of covariances), passing to the frequency domain is not pursued. Effectively, the study of wave motion has to be carried out directly in the time domain, just as recently employed in the in-plane stochastic Lamb's problem [34]. Therefore, our strategy involves running numerical solutions of the transient wave problem on realizations of the RF, and repeating them in the Monte Carlo sense in order to assess the statistics of responses.

Note that Cauchy and Dagum covariance functions make it impossible to obtain explicit analytical solutions even for one-dimensional elasostatic problems of random rods and beams under random forcings, and one has to resort to numerics [51, 54]. On the other hand, assuming such covariance functions for random process loadings of linear dynamical systems (such as the damped harmonic oscillator) does admit some explicit solutions for the response [53]. This chapter is organized as follows: section 2.1 introduces cellular automata (CA) algorithm for anti-plane problems. Section 2.2 describes the classical anti-plane shear Lamb's problem, its theoretical solution and the modeling parameters. Section 2.3 and Section 2.4 presents the dynamic responses for the homogeneous medium and RFs, respectively. Finally, Section 2.5 gives the conclusions.

2.1 Cellular cutomata for anti-plane problem

2.1.1 The physics-based model

Cellular Automata (CA) is a physics-based computational method, which was first proposed and implemented by John von Neumann [58]. Recently, Leamy *et al.* [17, 20] adapted this method to study the in-plane elastodynamics in a linear elastic medium using rectangular and non-uniform triangular meshes. Their rectangular-celled CA is mathematically equivalent to a central finite difference method, while CA directly discretizes the domain, and avoids deriving the governing partial differential equations of classical elasticity. CA would also require different stress assignment and boundary condition treatment. This section aims to detail the CA approach for anti-plane shear Lamb's problem in terms of external and inner shear force, balance of momentum, boundary condition and the Euler stepping algorithm while incorporate spatial randomness in mass density field for each cell.

As shown in figure 2.1(a), CA discretizes the computational domain into cells and the state of each cell depends on the cells that share an edge with this cell. For anti-plane problem, its displacement, velocity and external force define the cell state. The only non-zero components are in the z direction: displacement u_z, velocity v_z, and external force F_z. All of them are functions of x and y. Analogous to the in-plane development in [20], we have the anti-plane formulations for the shear forces calculated for the cell (i, j)

$$F_z^{top} = (w\Delta x)\sigma_{yz}^{top} = (w\Delta x)\mu\frac{^{i,j+1}u_z - ^{i,j}u_z}{\Delta y}, \tag{2.3a}$$

$$F_z^{bottom} = (w\Delta x)\sigma_{yz}^{bottom} = (w\Delta x)\mu\frac{^{i,j}u_z - ^{i,j-1}u_z}{\Delta y}, \tag{2.3b}$$

$$F_z^{right} = (w\Delta y)\sigma_{xz}^{right} = (w\Delta y)\mu\frac{^{i+1,j}u_z - ^{i,j}u_z}{\Delta x}, \tag{2.3c}$$
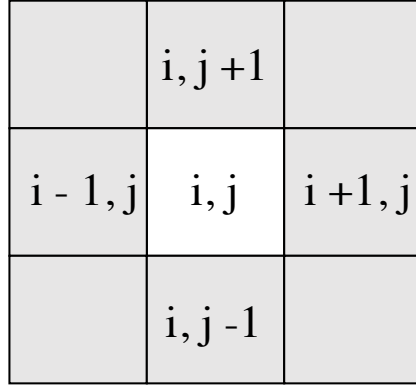
(a) cell (i,j) of CA
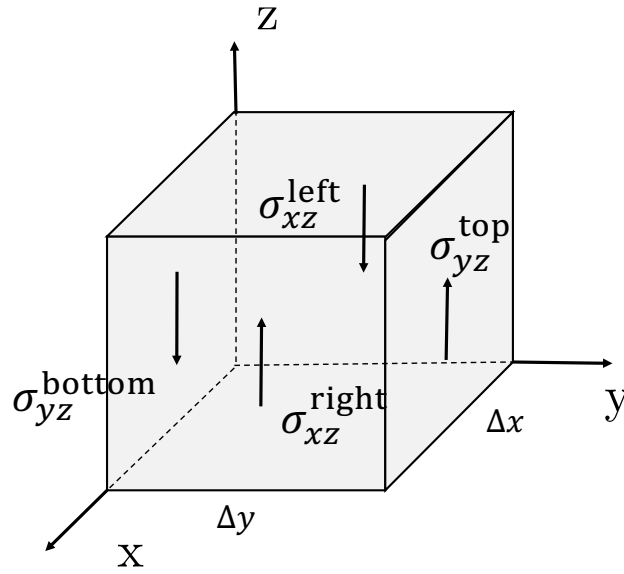
(b) Neighbor stresses on cell(i,j)

Figure 2.1: (a) cell (i,j) and its neighbors on cellular automata discretization (b) the neighbor stresses acting on cell(i,j).

$$F_z^{left} = (w\Delta y)\sigma_{xz}^{left} = (w\Delta y)\mu\frac{{}_{i,j}u_z - {}_{i-1,j}\,u_z}{\Delta x}, \tag{2.3d}$$

where w is the width in the z direction, while Δx and Δy are cell spacings in x, y directions, respectively.

The balance of linear momentum in the z direction, see figure 2.1(b) for the cell (i,j) gives

the relationship

$$\rho w \Delta x \Delta y \dot{v}_z = F_z^{external} + (F_z^{right} + F_z^{top} - F_z^{left} - F_z^{bottom}), \tag{2.4}$$

Similar to the in-plane problem [20] we introduce an integer m representing number of steps per second, so that, for each time step, we can update the velocity at $(k+1)$st step based on the kth step as

$$v_z^{k+1} = v_z^k + \frac{1}{m\rho w \Delta x \Delta y}[F_z^{external} + (F_z^{right} + F_z^{top} - F_z^{left} - F_z^{bottom})], \tag{2.5}$$

The displacement for the next time step is updated using the number of steps correspondingly as

$$u_z^{k+1} = u_z^k + \frac{1}{m}v_z^{k+1}, \tag{2.6}$$

Finally, the CA requires two common boundary conditions. The first is the free surface boundary condition: the free surface is modeled by adding an additional layer of cells, for which the stresses on the matching face are enforced to be zero. The second is Dirichlet (or first-type) boundary conditiont where the displacement and velocity boundary conditions can be prescibed directly. For anti-plane shear wave problem, the free surface condition gives:

$$_{i,1}\sigma_{yz}^{bottom} = \mu\frac{_{i,1}u_z - _{i,0}u_z}{\Delta y} = 0, \tag{2.7}$$

which means the desired condition is $_{i,0}u_z = _{i,1}u_z$.

2.1.2 Time stepping algorithm

The Euler method [20] is used to advance in time and update the cell state, which is given in Table 2.1. The mass density at point (i,j) is $\rho(i,j)$, and at time step q, the internal force is $F_z^{internal}(i,j)$. The external force is $F_z^{external}(i,j)$ Velocity is given by $v_z^n(i,j)$ and

Table 2.1: Euler method for anti-plane Lamb's problem.

Step 1:	$v_z^{q+1}(i,j) = v_z^q(i,j) + \frac{\Delta t}{\rho(i,j)\Delta x \Delta y \Delta z}\left(F_z^{\text{internal}}(i,j) + F_z^{\text{external}}(i,j)\right)$
Step 2:	$u_z^{q+1}(i,j) = u_z^q(i,j) + \Delta t v_z^{q+1}(i,j)$
Step 3:	Update F_z^{internal}

deformation is $u_z^n(i,j)$.

2.2 The classical anti-plane Lamb's problem

The classic in-plane Lamb's problem has been studied both theoretically and experimentally [1,7,45]. The in-plane Lamb's problem on random mass density fields with fractal and Hurst effects has been studied numerically in [32–34] and its displacement responses under random mass density fields will be discussed in the next chapter. Both pressure (P) and Rayleigh (R) waves have been considered. The present study concentrates on the shear wave responeses and its sensitivity analysis.

We use the same material properties as in Dally's experimental study [7] and Nishawala's numerical simulation [34]: the material is CR-39 with Young's modulus 3.85 Gpa (559ksi), Poisson's ratio 1/3, and mass density $1,300\ kg/m^3$. It follows that the shear wave speed is $1,054$ m/s.

The computational domain and loading condition can be found in Fig. 2.2(a) and Fig. 2.2(b), respectively. Consistent with [34], the width and height are set to be 0.39 m and 0.195 m, respectively, with a spacing in z direction (thickness) being 6.655 mm. A triangular inpulse load in Fig. 2.2(b) is applied at the origin. This impluse load has an amplitude of 20.7 kN and a width of 20 μs. For this study, we consider the displacement and stress responses up to the time 92 μs, i.e. the shear wave does not yet reach the domain boundary.

Kausel's studies [18] give the theoretical solutions for such anti-plane elastic shear wave propagation with a unit impulse line load in Chapter 5. The displacement response with

(a) Computational domain

(b) Triangular impulse load
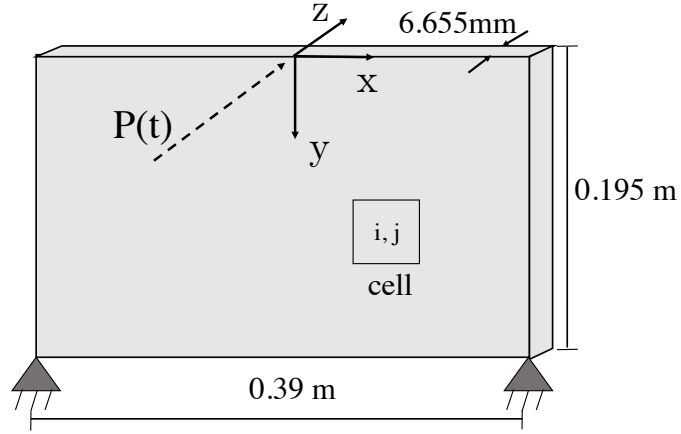
Figure 2.2: (a) Computational domain (b) Anti-plane triangular load.

respect to x and t, at $y = 0$, reads:

$$u_z(x, t) = \frac{P\gamma}{\pi\mu|x|} \frac{1}{\sqrt{\tau^2 - 1}} \mathcal{H}(\tau - 1) \tag{2.8}$$

where P represents an impulsive anti-plane line source applied at $x = y = z = 0$ with dimensions $[F][T]/[L] = [\text{impulse}][\text{length in z direction}]$. Here γ and μ are the shear wave speed and shear modulus, respectively, τ is defined as: $t\gamma/|x|$, and $\mathcal{H}$ denotes the Heaviside step function.

This impulse response is also known as the Green function for this specific problem. We can

22

then find a more general displacement response at $t = t_1$ for any time-dependent loading $P(t)$ as:

$$u_z(x) = \int_0^{t_1} \frac{P(t)\gamma}{\pi\mu|x|} \frac{1}{\sqrt{\tau^2 - 1}} \mathcal{H}(\tau - 1)dt. \tag{2.9}$$

The above theoretical results are next compared with computational dynamic responses obtained on homogeneous field and random mass density fields with both Cauchy and Dagum random fields.

2.3 Homogeneous results

We start our numerical validation with homogeneous results. This section evaluates the displacement and stress responses with homogeneous mass density and studies the convergence of cellular automata as the meshes refine.

The computational domain in figure 2.2 is firstly discretized with N_x=256 cells in the x direction and $N_y = 128$ nodes in the y direction. Then we refine the mesh with double nodes in both directions until the finest mesh has 2,048 nodes in the x direction and 1,024 nodes in the y direction. A timestep of 0.125 μs is speficied for all four mesh settings. We focus on the right half-plane only since the domain is symmetric.

Figure 2.3 shows that as the meshes become finer, the match of CA-predicted results, in terms of both shape and location, with the theoretical solution for both displacement and stress improves. However, the results for $N_x = 1,024$ and N_x overlap, which suggests that CA sufficiently converges at N_x=1,024 and there is no need to further refine the mesh. This makes sense because they are both essentially derived from the same governing equation for anti-plane shear wave.

Theoretical solution and CA responses of $N_x = 1024$ and $N_y = 512$ serve as benchmarks for random fields response and will be refered as the "Theoretical" and "CA homogeneous", respectively.
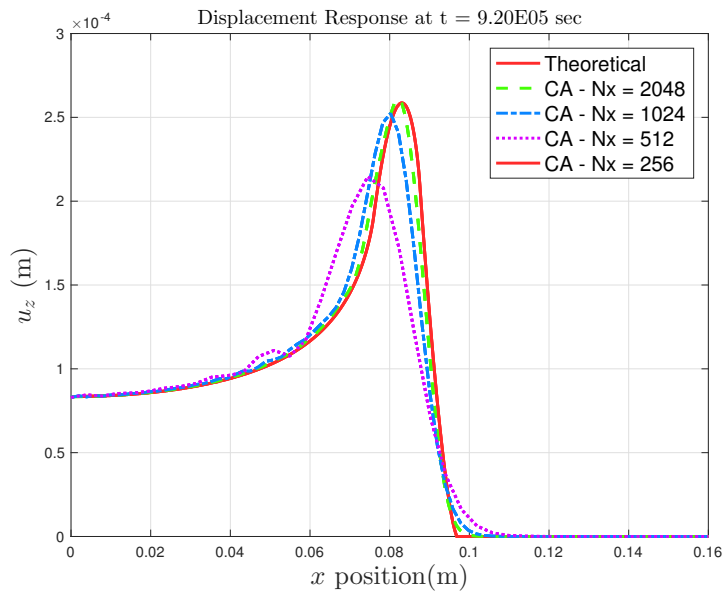
(a) Displacement responses
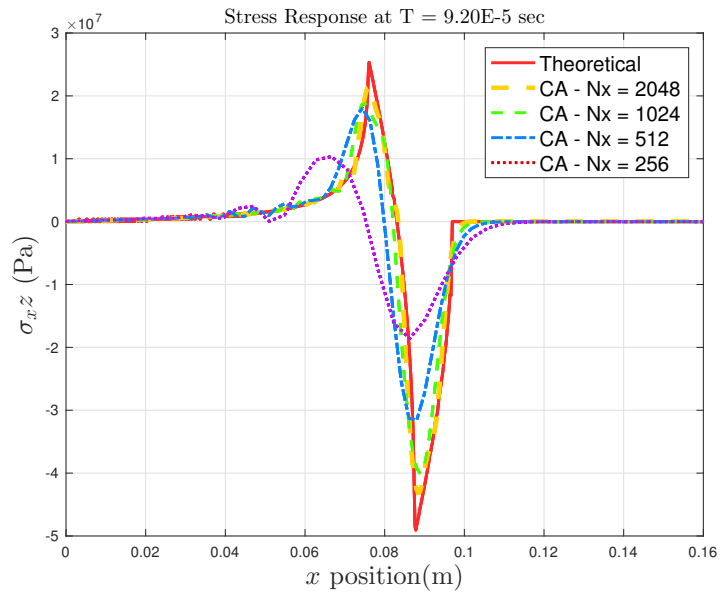
(b) Stress σ_{xz} responses

Figure 2.3: At 92μs: CA surface displacement and stress responses for anti-plane

2.4 Random fields results and discussion

2.4.1 Cauchy random field responses

This section first visualizes the nine different Cauchy RFs with the same mean $\langle \rho \rangle = 1,300$ kg/m^3 and CV$_{\mathrm{RF}} = 0.124$. Then the responses of RFs with $\alpha = 1.8$ ($D = 2.1$) and three varying βs were ploted and analyzed in detail. Finally, the effects of fractal and Hurst coefficient on SNR$_{\mathrm{R}}$ are stated based on a contour plot comparing SNR$_{\mathrm{RF}}$ and SNR$_{\mathrm{R}}$ with varying α and β.
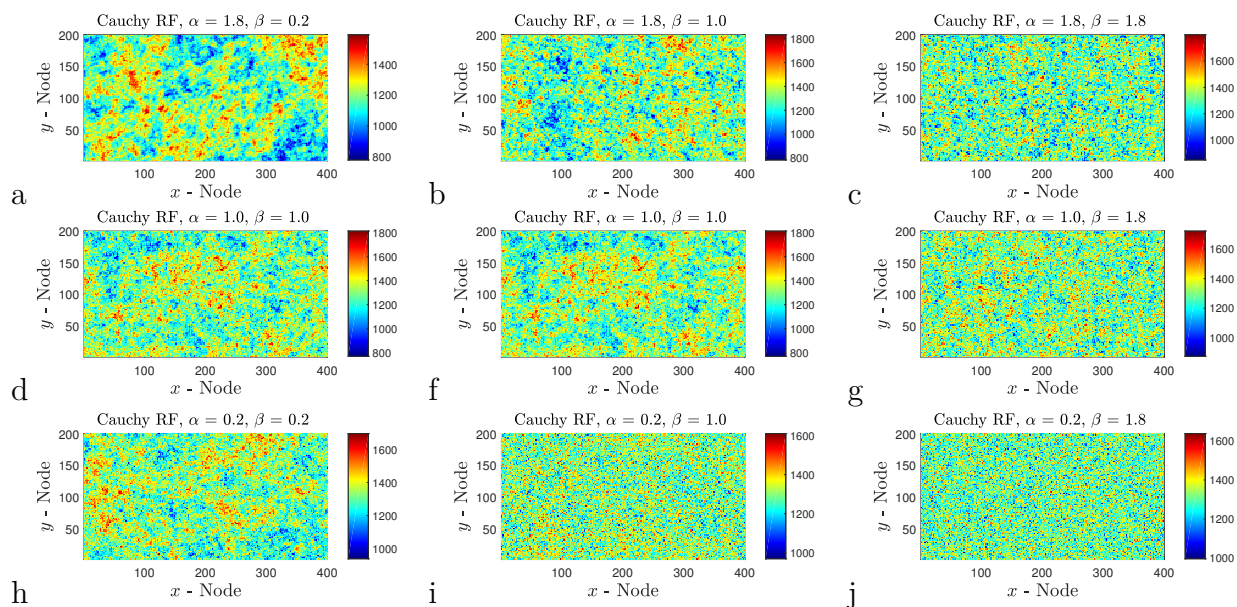
Figure 2.4: Cauchy mass RFs with mean = 1300 kg/m^3 and CV$_{\mathrm{RF}} = 0.124$, (a,d,g) $\beta = 0.2$; (b,f,i) $\beta = 1.0$; (c,f,i) $\beta = 1.8$. (a,b,c) $\alpha = 1.8$; (d,f,g) $\alpha = 1.0$; (h,i,j) $\alpha = 0.2$.

Figure 2.4 plots realizations of Cauchy RF for nine different α and β combinations. It is clear here that the region tends to be "tougher" for higher α and lower β values (the top-left area) and the region tends to be more uniformly distributed has lower α and higher β values (the bottom-right area). For RFs with "tougher" regions, we can consider the realization coarser. Figure 2.5 shows the mean and s.d. of the 128 realizations with $\alpha = 1.8$ ($D = 2.1$) and $\beta = 0.2, 1.0, 1.8$ for surface displacements at $y = 0$ in the x-direction shown in Figure 2.2, respectively. The theoretical solution and homogenerous CA results are also plotted

(a)

(b)

(c)
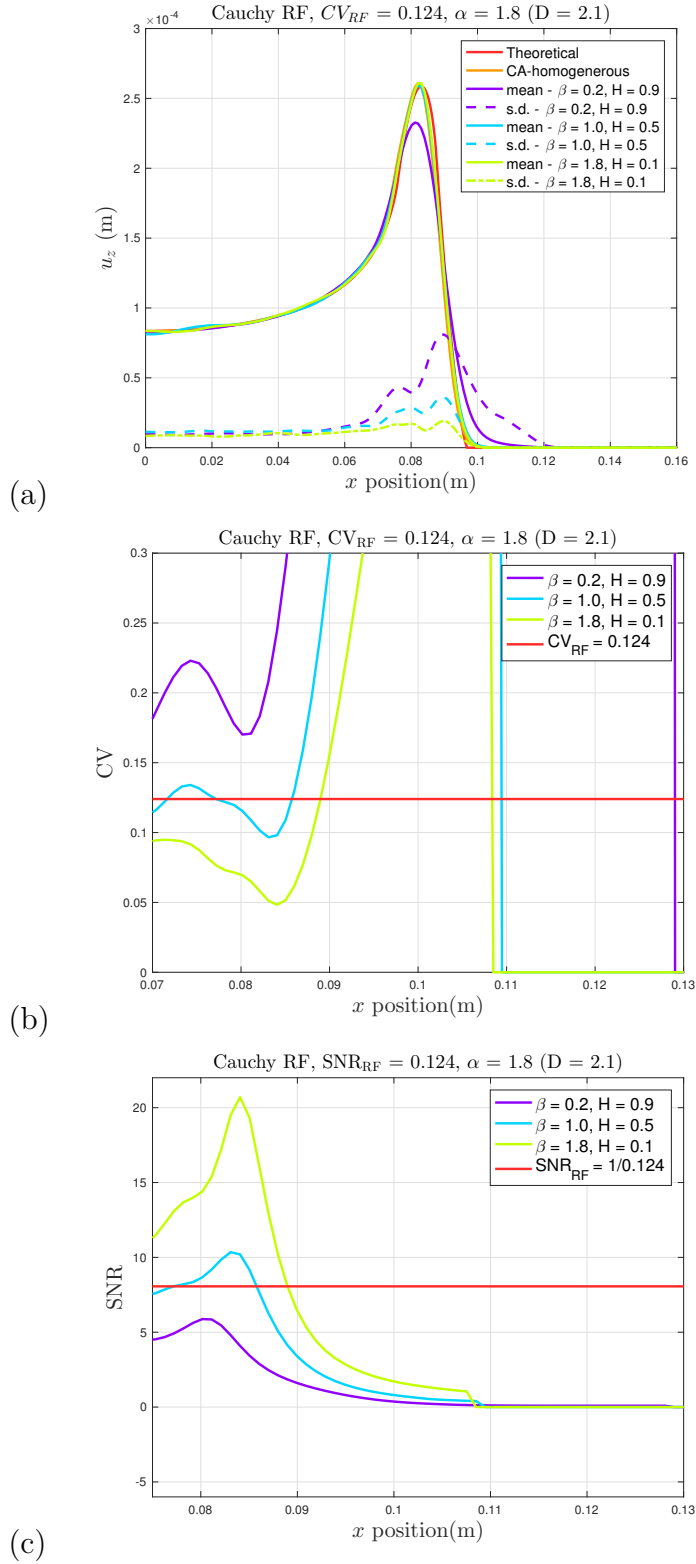
Figure 2.5: Cauchy anti-plane RFs surface displacement responses at $y = 0$ with $\alpha = 1.8$ (D = 2.1) and varying β. (a): mean and s.d. of random fields responses versus theoretical solutiona and homogenerous results; (b) CV of response versus CV of RF; (c) SNR of response versus SNR of RF.

Figure 2.6: Cauchy RFs with $CV_{RF} = 0.124$: anti-plane comparison of SNR_R and SNR_{RF} for varying α and β. The boundary between SNR_R less than or greater than SNR_{RF} is roughly represently by the dotted line.

in the same figure for reference. Figures 2.5 also plots the CV_{RF} and SNR_R. As we can see, as β increases, the mean becomes closer to the theoretical solution and the standard deviation decreases, which results a decreasing CV_{RF} and an increasing SNR_R. This can be explained since a bigger β (smaller H) correspondes to a finer RF realization. We also evaluated reponses for several fixed βs, but no significalnt trend can be found while varying α.

We also see that for $\beta = 0.2$, the $CV_R > CV_{RF}$ while for $\beta = 1.0$ and 1.8, the $CV_R < CV_{RF}$. The boundary between CV_{RF} being 'less than' or 'greater than' is determined by a comprehensive evaluation of other combinations of α and β. Considering there are regions where the mean response is close or equal to zero, we compare SNR_R and SNR_{RF} to evaluate the fractal and Hurst effects.

Figure 2.6 shows the comparison of SNR_R and SNR_{RF} for varying α and β. A 'x' indiactes the maximum of SNR_R at this combination of α and β is less than SNR_{RF} while an 'o' means the maximum of SNR_R at this combination of α and β is greater than SNR_{RF}. The approximate boundary between the "less than" and "greater than" regions is represented by a dotted line.

Compared with pressure and Rayleigh waves in Nishawala's work, we see that the effects of fractal dimension and Hurst parameter on the shear wave are similar in the sense that the response is less senstive for lower Hurst paramters. But, in general, the displacement response is also less sensitive for shear behaviors if we have the same fractal and Hurst paramter settings.

2.4.2 Dagum random field response

Similarly, this section deals with Dagum RFs with the same mean $\langle \rho \rangle = 1,300$ and $\text{CV}_{\text{RF}} = 0.124$. Figure 2.7 plots nine different Dagum RFs. The responses of RFs with $\alpha = 0.8$ ($D = 2.6$) and varying β were plotted and analyzed in detail. The effects of fractal and Hurst coefficient on SNR_{R} are evaluated based on a comprehensive comparison of SNR_{RF} and SNR_{R}, which is shown by a contour plot with varying α and β.
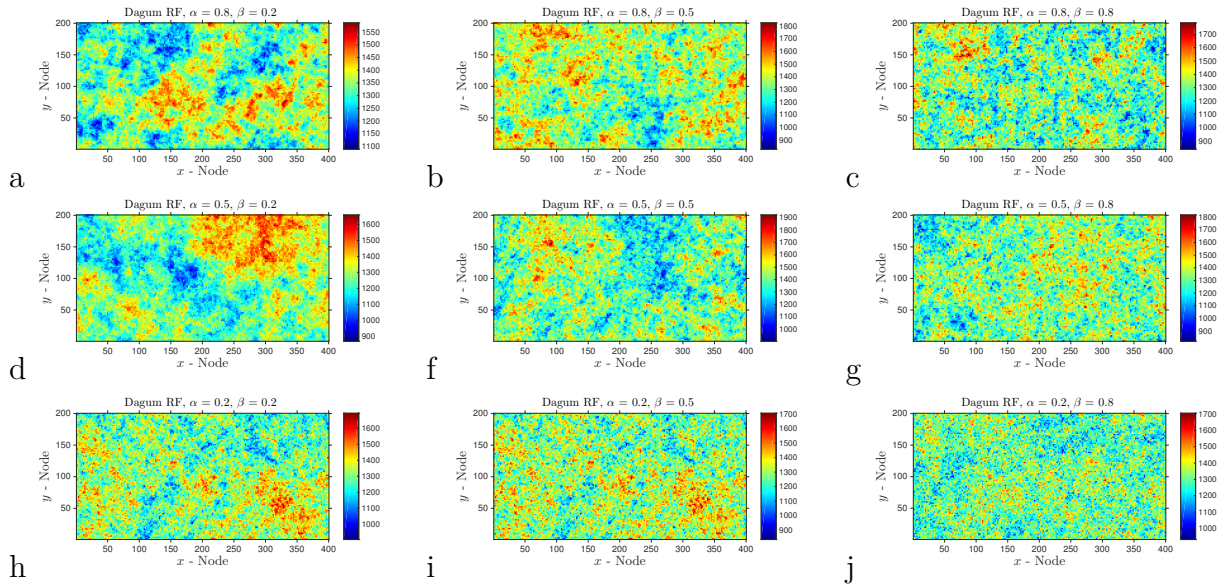
Figure 2.7: Dagum mass RFs with $\langle \rho \rangle = 1,300$ kg/m^3, $\text{CV}_{\text{RF}} = 0.124$

Figure 2.8 shows the mean and s.d. of the 128 realizations with $\alpha = 0.8$ ($D = 2.9$) and $\beta = 0.2, 0.5, 0.8$ for surface displacements at $y = 0$ in the x-direction shown in Figure 2.2, respectively. The theoretical solution and homogenerous CA results are also plotted in the same figure for reference. Figure 2.8 also plots the CV_{RF} and SNR_{RF}. As β increases, the
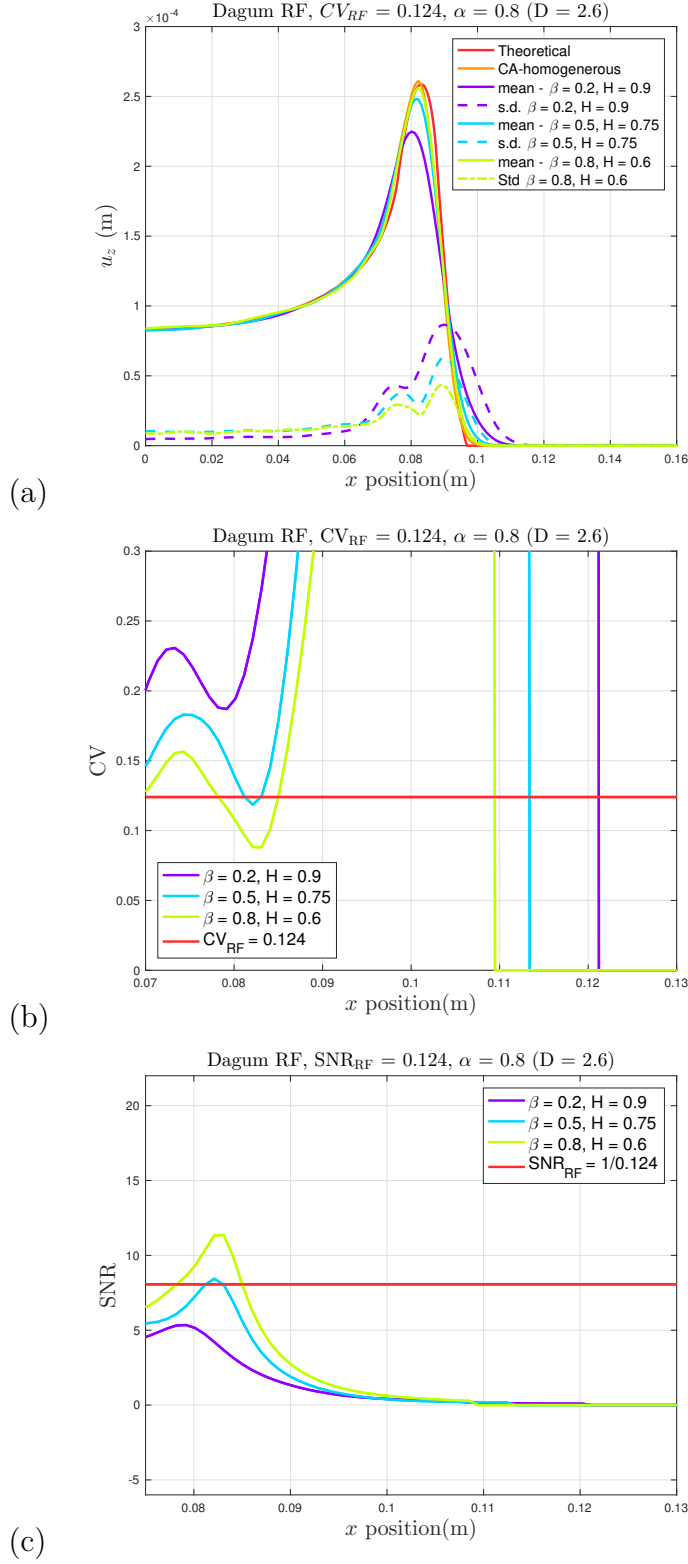
Figure 2.8: Dagum RFs anti-plane surface displacement responses at $y = 0$ with $\alpha = 0.8$ (D = 2.9) and varying β. (a): mean and s.d. of random fields responses versus theoretical solutiona and homogenerous results; (b) CV of response versus CV of RF; (c) SNR of response versus SNR of RF.
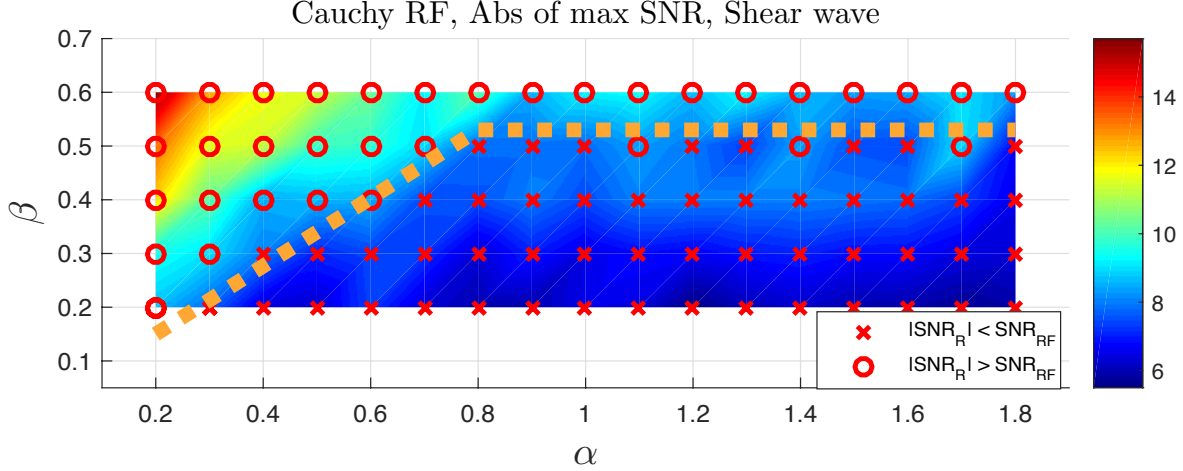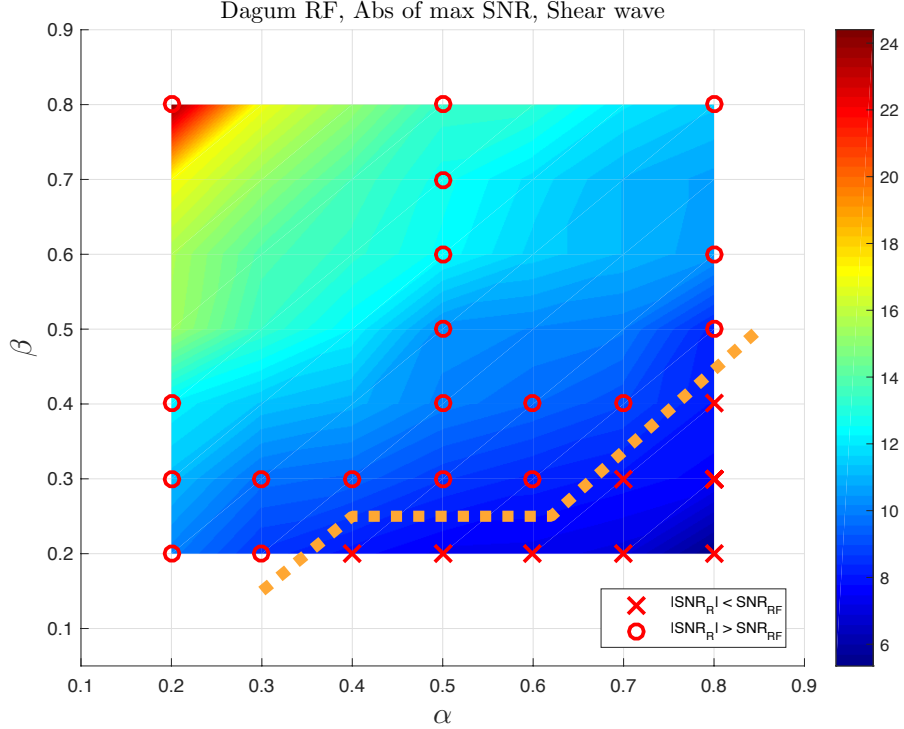
Figure 2.9: Dagum RFs with $\mathrm{CV_{RF}} = 0.124$: anti-plane comparison of $\mathrm{SNR_R}$ and $\mathrm{SNR_{RF}}$ for varying α and β. The boundary between $\mathrm{SNR_R}$ less than or greater than $\mathrm{SNR_{RF}}$ is roughly represently by the dotted line.

mean becomes closer to the theoretical solution and the standard deviation decreases, which results in a decreasing $\mathrm{CV_{RF}}$ and an increasing $\mathrm{SNR_{RF}}$. This can be explained since a larger β (smaller H) correspondes to a finer random field realization. We also evaluate the reponses for several fixed βs but again no significant trend can be found while varying α.

Similarly, with Cauchy RFs, Figure 2.9 shows the comparison of $\mathrm{SNR_R}$ and $\mathrm{SNR_{RF}}$ for varying α and β for Dagum RFs. A 'x' indicated the maximum of $\mathrm{SNR_R}$ at this combination of α and β is less than $\mathrm{SNR_{RF}}$ while an 'o' means the maximum of $\mathrm{SNR_R}$ at this combination of α and β is greater than $\mathrm{SNR_{RF}}$. Results of Figure 2.9 are qualitatively the same and quantitatively very similar to those of [33].

2.5 Summary

This chapter analyzes the anti-plane shear Lamb's problem on random mass density fields with fractal and Hurst effects. The study is of great practical importance since fractal and Hurst characteristics can be found in many patterns in nature and are used to quantify the spatial randomness in material properties. Cellular Automata (CA) is used to approach the dynamics responses in random mass density fields. Solutions incorporating spatical fluctuations are compared with classical theoretical solution and homogenerous simulation results. In general, the study finds out that for fields with smaller Hurst parameter (finer mesh), the mean responses of 128 realizations is closer to the theoretical solution.

A comprehensive evaluation of different combinations of fractal dimension and Hurst effects is carried out for both Cauchy and Dagum RFs. We focus the evaluation on stochastic imperfection senstivity by comparing the signal-to-noise ratio of the response (SNR_R) to the signal-to-noise ratio of RF (SNR_RF).

Overall, for smaller β (higher H), SNR_R is lower than SNR_RF, which is expected since higher H corresponds to a coarser field realization. For Cauchy field, when α is large enough, it seems the relationship is independent of α with SNR_R being less than SNR_RF. For Dagum field, there is still some changes in the relationship even though α is large enough. For larger β (lower H), the mean response of RFs would be very close to the homogenerous simulation, which results in SNR_R being greater than SNR_RF. SNR_R increases when β increases.

In general, for Cauchy RFs, for β values greater than 0.51, SNR_R is less than SNR_RF. For Dagum field, the boundary locates where β is approximately 0.25. Compared with pressure and Rayleigh wave behavior in the same random media, we find that the fractal dimension still has a less significant effect than the Hurst parameter. Also, for random mass density fields with the same fractal and Hurst characteristics, the shear wave is less sensitive to spatial fluctuations compared with pressure and Rayleigh waves.

Chapter 3

In-plane Lamb's problem on random mass density fields[1]

We now move to vector solution responses. This chapter reports the application of cellular automata (CA) to study the dynamic responses of Lamb-type problems for a tangential point load and a concentrated moment applied on the free surface of a half-plane. Analog to anti-plane Lamb's propagation, the medium is homogeneous, isotropic linear elastic while having a random mass density field with fractal and Hurst characteristics. Both Cauchy and Dagum random field models are used to capture these effects [65].

Cellular automata is modified from anti-plane since the local updating algorithm is evolved. The CA approach is reframed in this chapter and verified on progressively refined meshes in a homogeneous continuum and random media with white noise.

The governing differential field equation for an in-plane wave propagation is replaced by a stochastic field equation incorporating the randomness of the operator

$$\mathcal{L}(\omega)\mathbf{u} = f; \quad \omega \in \Omega. \tag{3.1}$$

$$\begin{bmatrix} \dot{v} \\ \dot{r} \end{bmatrix} = \begin{bmatrix} -\frac{C_{\alpha f}+C_{\alpha r}}{mu} & -\frac{aC_{\alpha f}+bC_{\alpha r}}{mu} - u \\ \\ -\frac{bC_{\alpha r}-aC_{\alpha f}}{Iu} & -\frac{a^2C_{\alpha f}+b^2C_{\alpha r}}{Iu} \end{bmatrix} \begin{bmatrix} v \\ r \end{bmatrix} + \begin{bmatrix} \frac{C_{\alpha r}}{m} \\ \\ \frac{C_{\alpha r}}{I} \end{bmatrix} \delta \tag{3.2}$$

Here ω is a single event of the sample space Ω which together with a σ-algebra S and a probability measure P on it forms a probability space (Ω, S, P). Typically, a Gaussian mea-

---

[1]The content of this chapter is mostly taken out from our work in [65].

sure is assumed, although, if more information about the material randomness is available, a transformation to other types of probability distribution is possible. The space (Ω, S, P) defines a random medium $\mathcal{B} = \{B(\omega); \omega \in \Omega\}$.

Overall, this paper is organized as follows. Section 3.1 formulates the problem by introducing the concepts and stepping algorithms for in-plane cellular automata. Section 3.2 introduce and present the classical, theoretical in-plane problems under a tangential and a concentrated moment problem. section 3.3 and section 3.4 present homogeneous and RFs results, respectively. Finally, Section 3.5 concludes this study.

3.1 Cellular automata for in-plane problem

Similar to cellular automata (CA) for anti-plane, CA for in-plane elastodynamics also use rectangular meshes. The state of each rectangular cell not only depends on the state of cells that share an edge, but also depend on the state of cells that share a vertex with the cell. The cell's deformation and velocity, in both the x and y directions, are defined as the cell's state. In CA, traction boundary conditions require an additional layer of cells assigned to the defined stress. Displacement boundary conditions are assigned directly. The section presents the local updating rules and stepping algorithms of cellular automata for in-plane problem.

3.1.1 The physics-based model

For convenience, we introduce the following abbreviation for finite difference operators,

$$D_x\left[u_m(i,j)\right] = \frac{u_m(i+1,j) - u_m(i-1,j)}{2\Delta x}, \tag{3.3}$$

and

$$D_y\left[u_m(i,j)\right] = \frac{u_m(i,j+1) - u_m(i,j-1)}{2\Delta y} \tag{3.4}$$

33

where (i, j) denote the position of a particular CA cell, m is either x or y direction. u_x and u_y are the x and y component of the displacement solution field.

Reproduced from [20], the balance of linear momentum in the y direction for homogeneous field generates

$$\rho \Delta x \Delta y \Delta z \dot{v}_y = F_y^{\text{external}} + \left(F_y^{\text{right}} + F_y^{\text{top}} - F_y^{\text{left}} - F_y^{\text{bottom}} \right) = F_y^{\text{external}} + F_y^{\text{internal}} \quad (3.5)$$

where $\Delta x, \Delta y, \Delta z$ represent the grid spacing and ρ is the mass density. F_y^{top} denotes the tensile force on the top face, which is given by the relationship

$$F_y^{\text{top}} = \Delta x \Delta z \left[\frac{\lambda + 2\mu}{\Delta y} \left(u_y(i, j+1) - u_y(i, j) \right) + \frac{\lambda}{2} \left(D_x \left[u_x(i, j+1) \right] + D_x \left[u_x(i, j) \right] \right) \right] \quad (3.6)$$

where λ and μ are the Lamé's parameters of the homogeneous field.
F_y^{bottom} denotes the tensile force on the bottom face, which is given by the relationship

$$F_y^{\text{bottom}} = \Delta x \Delta z \left[\frac{\lambda + 2\mu}{\Delta y} \left(u_y(i, j) - u_y(i, j-1) \right) + \frac{\lambda}{2} \left(D_x \left[u_x(i, j-1) \right] + D_x \left[u_x(i, j) \right] \right) \right]$$
$$(3.7)$$

The shear forces on the right and left faces are represented by F_y^{right} and F_y^{left} respectively. They are given by:

$$F_y^{\text{right}} = \Delta y \Delta z \left[\mu \frac{u_y(i+1, j) - u_y(i, j)}{\Delta x} + \frac{\mu}{2} \left(D_y \left[u_x(i+1, j) \right] + D_y \left[u_x(i, j) \right] \right) \right] \quad (3.8)$$

and

$$F_y^{\text{left}} = \Delta y \Delta z \left[\mu \frac{u_y(i, j) - u_y(i-1, j)}{\Delta x} + \frac{\mu}{2} \left(D_y \left[u_x(i-1, j) \right] + D_y \left[u_x(i, j) \right] \right) \right] \quad (3.9)$$

Table 3.1: Euler Method for in-plane cellular automata.

Table 1.3: Euler Method	
Step 1:	$v_m^{q+1}(i,j) = v_m^q(i,j) + \frac{\Delta t}{\rho(i,j)\Delta x \Delta y \Delta z}\left(F_m^{\text{internal}}(i,j) + F_m^{\text{external}}(i,j)\right)$
Step 2:	$u_m^{q+1}(i,j) = u_m^q(i,j) + \Delta t v_m^{q+1}(i,j)$
Step 3:	Update F_m^{internal}

3.1.2 Time stepping algorithm

The Euler method [20] is used to advance in time and update the cell state, which is given in Table 3.1. The mass density at point (i,j) is $\rho(i,j)$, and at time step q, m means the x or y component and the internal force is $F_m^{\text{internal}}(i,j)$. The external force is $F_m^{\text{external}}(i,j)$. Velocity is given by $v_m^n(i,j)$ and displacement is given by $u_m^n(i,j)$.

3.2 Formulation of the problem

In this section, we first state the in-plane impact by a tangential load and in-plane implact by a moment problems in terms of their governing equation and their corresponding classical solution in homogeneous media. Then, we introduce randomness into the mass density field. Specifically, we are interested in random fields with fractal and Hurst effects. Finally, we provide the key relations of a CA algorithm, which are then used to simulate all the wave propagation problems.

3.2.1 Impact by a tangential load

For a homogeneous medium, the elastic wave fields are governed by the Navier (displacement) equation of motion:

$$(\lambda + \mu)\nabla\nabla \cdot \mathbf{u} + \mu\nabla^2\mathbf{u} + P(t)\delta(x)\delta(y) = \rho\frac{\partial^2 u}{\partial t^2};$$

$$\omega \in \Omega, \quad \mathbf{x} \in \mathbb{R}^2, \tag{3.10}$$
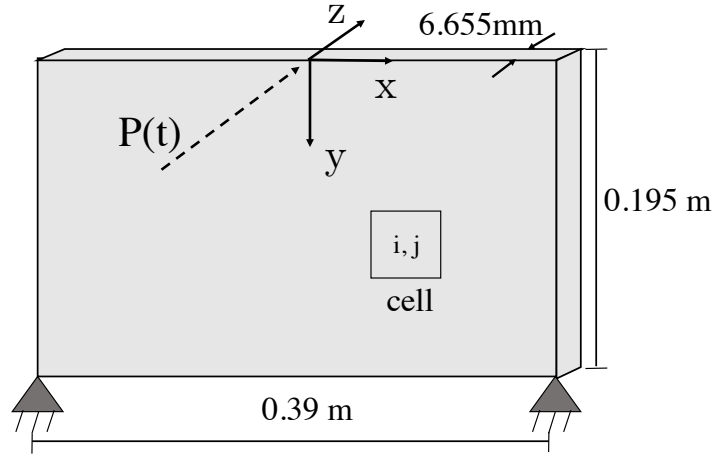
(a) (a) Problem definition

(b) (b) Triangular impulse load

Figure 3.1: Lamb-type problem with a concentrated tangential load $P(t)$ having a triangular history.

where $P(t)$ is the loading function, while λ and μ are the Lamé constants. The defined domain and the loading condition are sho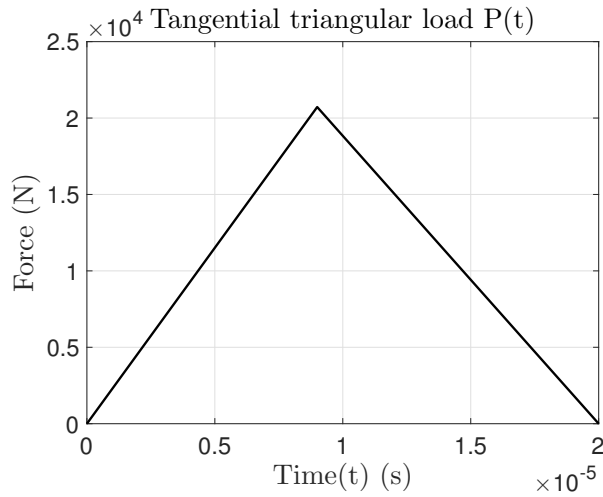wn in Fig. 3.1a and Fig. 3.1b, respectively. In order to benchmark with [34], the width and height are 0.39 m and 0.195 m, respectively, with a spacing in the z direction being 6.655 mm. A triangular impulse load in Fig. 3.1b is applied at the origin at $t = 0$. The amplitude and width of this impulse are 20.7 kN and 20 μs, respectively. We consider the displacement responses up to the time 92 μs, i.e. before the instant when the fastest wave would arrive at the domain boundary. Kausel's study [18] gives the theoretical solution for such a half-plane problem subjected to an impulsive in-plane

line source. Specifically, the x-component of displacement response at the surface ($y = 0$) reads:

$$u_x(x,t) = \frac{P\gamma}{\pi\mu|x|} \begin{cases} 0 & \text{if } \tau < a \\ \dfrac{4\tau^2(1-\tau^2)\sqrt{\tau^2-a^2}}{(2\tau^2-1)^4 + 16\tau^4(\tau^2-a^2)(1-\tau^2)} & \text{if } a \leqslant \tau \leqslant 1 \\ \dfrac{-\sqrt{\tau^2-1}}{(2\tau^2-1)^2 - 4\tau^2\sqrt{\tau^2-a^2}\sqrt{\tau^2-1}} & \text{if } \tau > 1, \end{cases} \qquad (3.11)$$

The physical dimension of P is $[\text{F}][\text{T}]/[\text{L}] = [\text{impulse}][\text{length in } z \text{ direction}]$. Here γ and μ are the pressure wave speed and the shear modulus, respectively, while $\tau := t\gamma/|x|$ and a denotes the ratio of the pressure wave speed to the shear wave speed.

This impulse response is the Green function for the problem. Henceforth, a more general displacement response at $t = t_1$ for any time-dependent loading $P(t)$ may be determined from

$$u_x(x) = \int_0^{t_1} P(t)u_x(x, t_1 - t)dt, \qquad (3.12)$$

3.2.2 Impact by a concentrated moment

Here, a concentrated moment $M(t)$ is applied to a half-plane, Fig. 3.2. This moment can be interpreted as a limiting case of a couple of finite magnitude, produced by two forces $F(t)$ of opposing directions, placed d apart, where d approaches zero while F goes to infinity [56]. The forces have a triangular impulse history. Consider F_1 to be a normal force applied to the right of the origin of the coordinate system at $(x, y) = (d/2, 0)$, while a force $F_2 = -F_1$ is applied to the left at $(x, y) = (-d/2, 0)$. The x-component of the displacement response at the surface due to either impulsive normal loading is given as [18]:

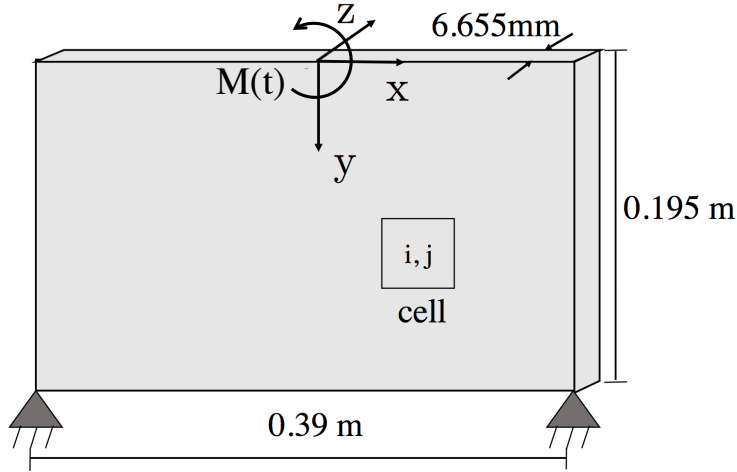$$u_{xk}(x,t) = \frac{(-1)^{k+1}F\gamma}{\pi\mu|x + (-1)^{k+1}\frac{d}{2}|}\Phi(\tau_k), \qquad (3.13)$$

Figure 3.2: Lamb-type problem with a concentrated moment.

with

$$
\Phi(\tau_k) = \begin{cases} \dfrac{2\tau_k(2\tau_k^2 - 1)\sqrt{\tau_k^2 - a^2}\sqrt{1 - \tau_k^2}}{(2\tau_k^2 - 1)^4 + 16\tau_k^4(\tau_k^2 - a^2)(1 - \tau_k^2)} & \text{if } a \leqslant \tau_k \leqslant 1, \\ \dfrac{\pi(2\tau_R^2 - 1)^3}{4(1 - 4\tau_R^2 + 8\tau_R^6(1 - a^2))} & \text{else,} \end{cases}
\tag{3.14}
$$

where $k = 1, 2$, $u_{x1}(x, t) := u_x|_{F_1}$ and $u_{x2}(x, t) := u_x|_{F_2}$. We have $\tau_1 := t\gamma/|x + \frac{d}{2}|$, $\tau_2 := t\gamma/|x - \frac{d}{2}|$ and $\tau_R := \frac{\beta}{C_R}$. Here γ and C_R are the pressure wave speed and Rayleigh-wave speed, respectively. μ and a denote the shear modulus and the ratio of the pressure wave speed to the shear wave speed.

The solution for M can then be obtained by superposing the solutions $u_{x1}(x, t)$ and $u_{x2}(x, t)$. The Green function for a concentrated moment is found by taking the limit $d \to 0$ and $F \to \frac{M}{d}$, while keeping $M = const$. With the help of Mathematica, we obtain the exact solution

$$u_x(x,t)|_{M(t)} = \frac{Mx^3\gamma^2 t}{\pi\mu}\sqrt{1-\tau^2}\sqrt{\tau^2-a^2}(2a^2x^{14}-4t^2x^{12}\gamma^2$$

$$+ a^2t^2x^{12}\gamma^2 + 23t^4x^{10}\gamma^4) - 97a^2t^4x^{10}\gamma^4 + 96a^4t^4x^{10}\gamma^4 - 9t^6x^8\gamma^6$$

$$+ 254a^2t^6x^8\gamma^6 - 144a^4t^6x^8\gamma^6 - 106t^8x^6\gamma^8 - 560a^2t^8x^6\gamma^8$$

$$+ 32a^4t^8x^6\gamma^8 + 384t^{10}x^4\gamma^{10} + 720a^2t^{10}x^4\gamma^{10} - 528t^{12}x^2\gamma^{12}$$

$$- 288a^2t^{12}x^2\gamma^{12} + 224t^{14}\gamma^{14}/\left[\left(x^2-t^2\gamma^2\right)\left(a^2x^2-t^2\gamma^2\right)\right.$$

$$\left.\left(x^8-9t^2x^6\gamma^2+24t^4x^4\gamma^4-16a^2t^4x^4z^4-16t^6x^2\gamma^6+16t^8\gamma^8\right)^2\right] \quad (3.15)$$

We again consider the displacement responses up to the time 92 μs. A more general displacement response at $t = t_1$ for any time-dependent loading $M(t)$ may be determined from

$$u_x(x) = \int_0^{t_1} M(t)u_x(x,t_1-t)dt \quad (3.16)$$

We again consider the displacement responses up to the time 92 μs. We use the same material properties for both loading cases as in Dally's experimental study [7] and Nishawala's numerical simulation [34]. The material is CR-39 with Young's modulus 3.85 GPa (559ksi), Poisson's ratio 1/3, and mass density 1,300 kg/m^3. It follows that the pressure wave speed is 1,826 m/s and Rayleigh wave speed is 969 m/s.

The theoretical solutions Eq. 3.12 and Eq. 3.16 will serve as references for responses of homogeneous (Section 3) and random (Section 4) media.

3.3   Response of a homogeneous medium

This section reports the convergence of the CA solution with increasing mesh refinement in the problem of a concentrated impact force on a homogeneous medium. First, the computational domain in Fig. 3.3 is discretized with $N_x = 256$ cells in the x direction and $N_y = 128$
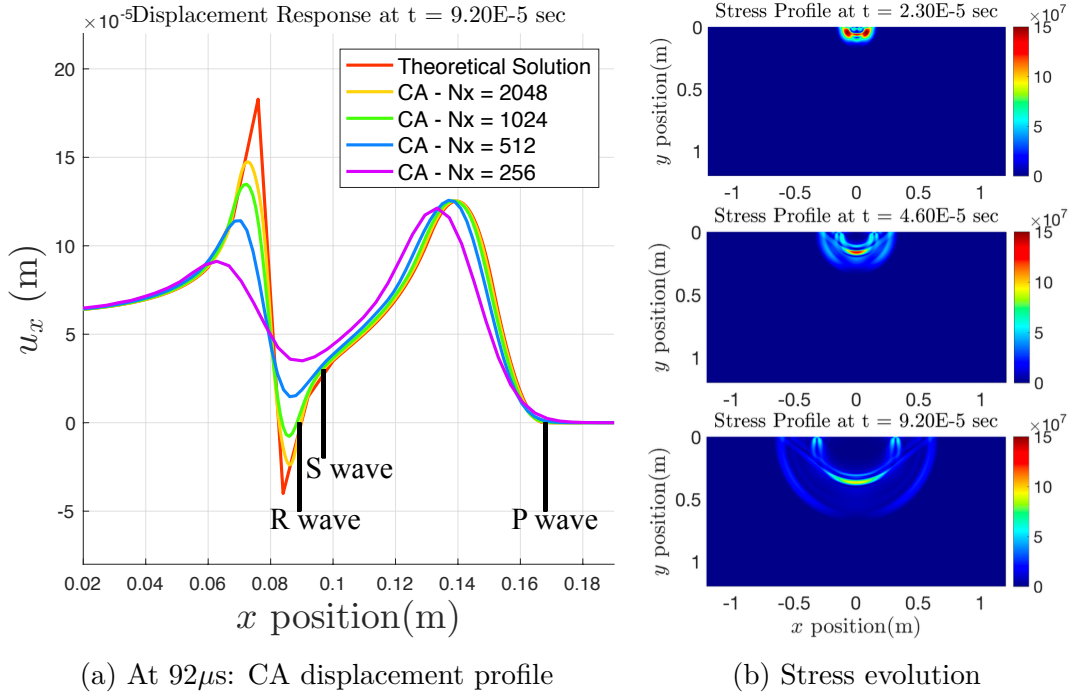
(a) At 92μs: CA displacement profile   (b) Stress evolution

Figure 3.3: (a) Convergence (with progressive mesh refinement $N_x = 256, ..., 2048$) of the CA solution to the thoretical solution in the concentrated tangential force problem, and (b) von Mises stress evolution on a mesh set at $N_x = 1024$.

nodes in the y direction. Then the mesh is refined by doubling nodes in both directions until the final mesh has $2,048$ nodes in the x direction and $1,024$ nodes in the y direction. A time step of 0.125 μs is held constant for all the cases. We only focus on the displacement responses of the right half-plane because the problem is symmetric.

Figure 3.3a shows the displacement in function of position on the free surface for these ever finer meshes. Clearly, as the meshes become finer, the CA-predicted displacement responses converge to the classical elastodynamics solution of (2.1), e.g [18]. The locations of wavefronts of the Rayleigh wave, shear wave, and pressure wave are indicated accordingly. To benchmark with [34, 64], we use $N_x = 1,024$ and $N_y = 512$ to simulate the wave propagation on mass density RFs.

The theoretical solution and CA responses for the homogeneous medium are used to compare with the average responses on RFs and will be referred to as the "Theoretical" and "CA homogeneous", respectively. Figure 3.3b shows the von Mises stress profiles for $N_x = 1,024$

and $N_y = 512$ at three different times. The stress intensity decreases as the wave propagates, according to geometric attenuation in 2d.

The same numerical settings are also applied to the problem with an applied pure moment. The same type of convergence of the CA solution towards the theoretical solution of Section 2.1.2, with increasing mesh refinement, is found for the concentrated moment problem.

3.4 Responses of random fields

3.4.1 RF results and discussion with a tangential load

This section focuses on the displacement responses for the Lamb problem of a half-plane subjected to a tangential impact load on both Cauchy and Dagum RFs. We use the same time step and mesh step for RF as the homogeneous mass density field. For the time step chosen, there is margin available to allow for higher and lower densities. Given our chosen time step $\delta t = 0.125 \mu s$, the minimum allowable mass density would be:

$$\rho_{min} = \frac{E\Delta t^2}{\Delta x^2 (1 - \nu^2)} = 7.28 \times 10^{-5} \text{kg/m}^3 \tag{3.17}$$

This is well below the lower bound of our symmetrically truncated-Gaussian RFs of mass density taking values within $\mu - 8\sigma \leq \rho \leq \mu + 8\sigma$ with the mean $\mu = 1,300$ and the standard deviation $\sigma = 161.2452$. Due to the nature of these random fields, as we refine the mesh, we should refine the random field along with it. Nishawala had evaluated random fields of varying coarseness in [33].

Cauchy random field responses

This section focuses on the displacement responses for Cauchy RFs of mass density under a tangential loading.

Figure 3.4.1 shows the surface displacement responses at $y = 0$ in the x-direction indicated in
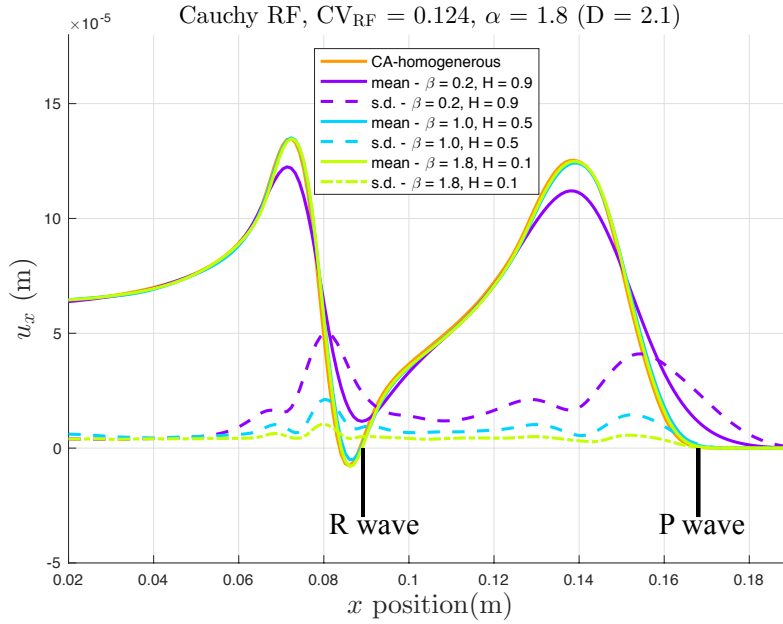
(a) Mean and s.d. of Cauchy RFs
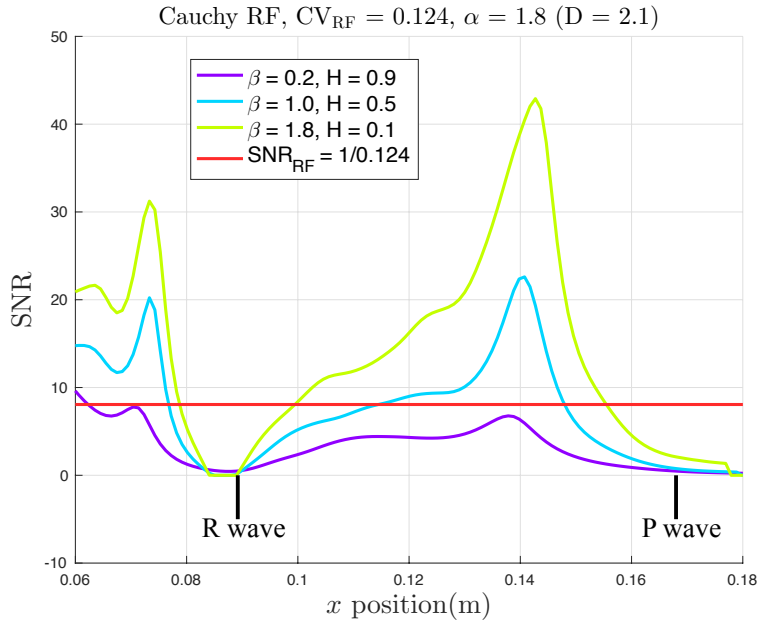
(b) SNR of response versus SNR of RF

Figure 3.4: Cauchy in-plane RFs tangential responses at $y = 0$ with $\alpha = 1.8$ ($D = 2.1$) and varying β. (a): mean and standard deviation (s.d.) of RFs responses versus homogeneous results; (b) SNR of response versus SNR of RF.

Figure 3.1a of RFs with $\alpha = 1.8$ ($D = 2.1$) and three values of βs. The mean and standard deviation of 128 realizations with $\alpha = 1.8$ ($D = 2.1$) and $\beta = 0.2, 1.0, 1.8$ are plotted

separately and are compared with homogeneous results shown in section 3.3. With reference to Figure 3.4b, as β increases, the mean becomes closer to the homogeneous results and the standard deviation decreases, which results in a smaller fluctuation and a larger $\mathrm{SNR_R}$. This is expected since a bigger β (smaller H) corresponds to a finer RF realization. On the other hand, when we fix β and vary α, no significant trend is found, which suggests that the Hurst parameter has a stronger effect on the responses than the fractal dimension.

Upon further analysis of the plots Figure 2.5, we can now answer the first question posed in the Introduction, i.e. relative to Eq. 1.4 and Eq. 1.5, in general, we have

$$\mathbf{u}_{\mathrm{det}} > \langle \mathbf{u} \rangle . \tag{3.18}$$

This is understood as the the loss of wave's amplitude (and energy) due to scattering and heterogeneities. However, the difference between these two quantities becomes smaller as the realization becomes smoother so we can consider $\mathbf{u}_{\mathrm{det}} = \langle \mathbf{u} \rangle$ when $\alpha > 1.0$ and $\beta < 0.1$.
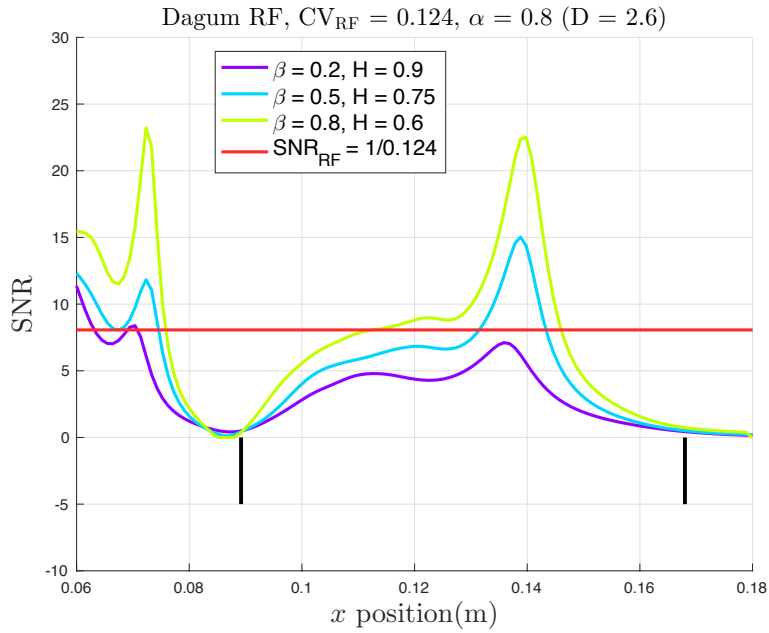
Dagum random field responses

Figure 2.7 presents nine different Dagum RFs with the same mean and $\mathrm{CV_{RF}}$ as those for Cauchy RFs. The average displacement responses of RFs with $\alpha = 0.8$ ($D = 2.6$) and varying βs are plotted in Figure 3.5. Finally a comprehensive evaluation of spatial fluctuations is presented by a contour plot with varying α and β. Note that only the upper left area where $\alpha < \beta$ from Figure 3.9 is permissible for Dagum RFs. We show all the combinations of fractal dimension and Hurst effects just for the completeness of this analysis.

Keeping α fixed while varying β, from plots Figure 3.5a, we see that, for larger β, the fluctuation of the responses is weaker, just as we observed it for Cauchy RFs. When we fix β and vary α, again, no significant trend is found. And this again answers the first question
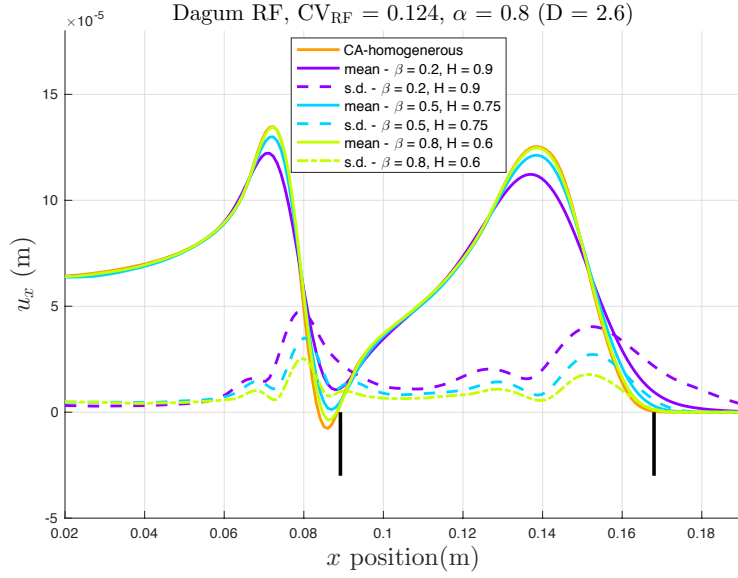
(a) Mean and s.d. of Dagum RFs

(b) SNR of response versus SNR of RF

Figure 3.5: Dagum in-plane RFs tangential responses at $y = 0$ with $\alpha = 1.8$ ($D = 2.1$) and varying β. (a): mean and standard deviation (s.d.) of random fields responses versus the homogeneous field results; (b) SNR of response versus SNR of RF.

posed in the Introduction, i.e, relative to Eq. 1.4 and Eq. 1.5:

$$\mathbf{u}_{\mathrm{det}} > \langle \mathbf{u} \rangle . \tag{3.19}$$

44

As before, this is due to the loss of wave's amplitude (and energy) due to scattering at heterogeneities; the difference becomes smaller as the realization gets smoother and we can approximately take $\mathbf{u}_{\text{det}} = \langle \mathbf{u} \rangle$ for all the permissible Dagum RFs.

### 3.4.2 RF results and discussion with a concentrated moment

This section focuses on the displacement responses for the problem with a concentrated moment on the same Cauchy and Dagum RFs.
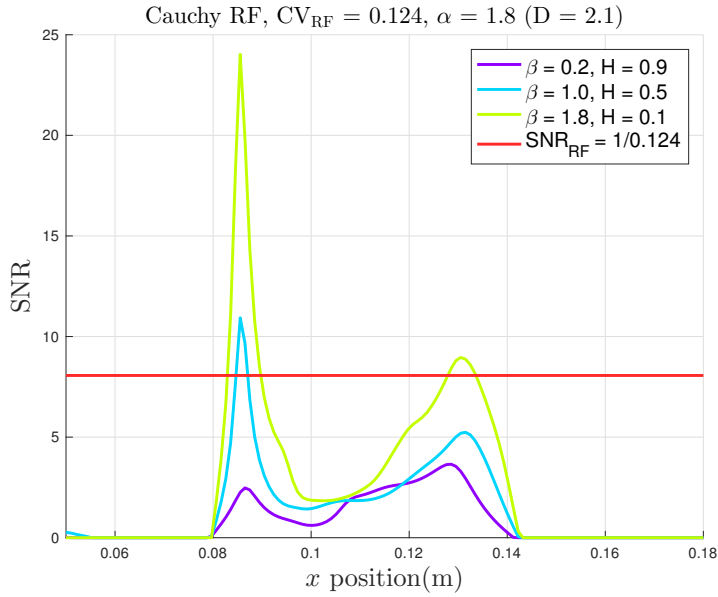
Cauchy random field responses

This section focuses on the displacement responses for the same Cauchy RFs of mass density indicated in Figure 2.4.

Figure 3.6a shows the responses at surface $y = 0$ of an applied moment with RFs with $\alpha = 1.8$ ($D = 2.1$) and three values of βs. The mean and standard deviation of 128 realizations with $\alpha = 1.8$ ($D = 2.1$) and $\beta = 0.2, 1.0, 1.8$ are plotted separately and are compared with the homogeneous results and theoretical solution. As β increases, the mean becomes closer to the homogeneous results and the standard deviation decreases, which results in a smaller fluctuation and a larger SNR_{R}, shown in Figure 3.6b. There are again two peaks for SNR corresponding to the P wave and Rayleigh wave. The Hurst parameter continues to have a stronger effect on the responses than the fractal dimension.

Figure 4.5 compares spatial sensitivity of pressure and Rayleigh waves with those in [34]. We find that the displacement responses of random media subjected to the tangential load are less sensitive to fractal and Hurst effects compared with those subjected to the normal load reported earlier. Responses of half-planes of the same random media under anti-plane shear load are drawn in this figure for reference and a more complete comparison.
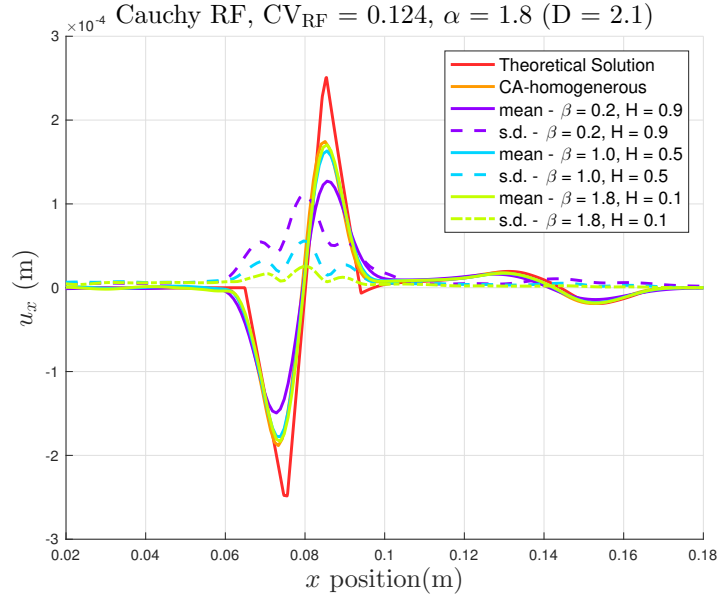
(a) Mean and s.d. of Cauchy RFs

(b) SNR of response versus SNR of RF

Figure 3.6: Pure moment responses: Cauchy RFs responses at $y = 0$ with $\alpha = 1.8$ (D = 2.1) and varying β. (a): mean and s.d. of random fields responses versus the homogeneous results; (b) SNR of response versus SNR of RF.

Dagum random field responses

Figure 3.8 shows the responses due to the applied moment with RFs with $\alpha = 1.8$ ($D = 2.1$) and three values of βs. The mean and standard deviation of 128 realizations with $\alpha = 0.8$
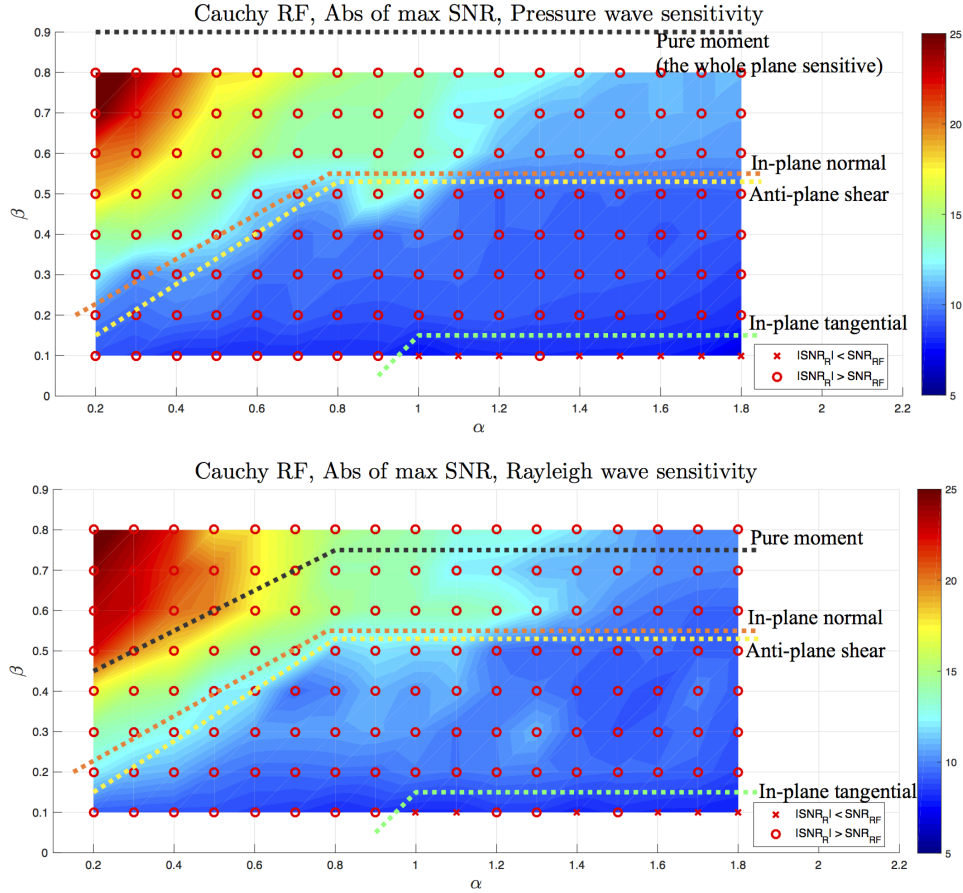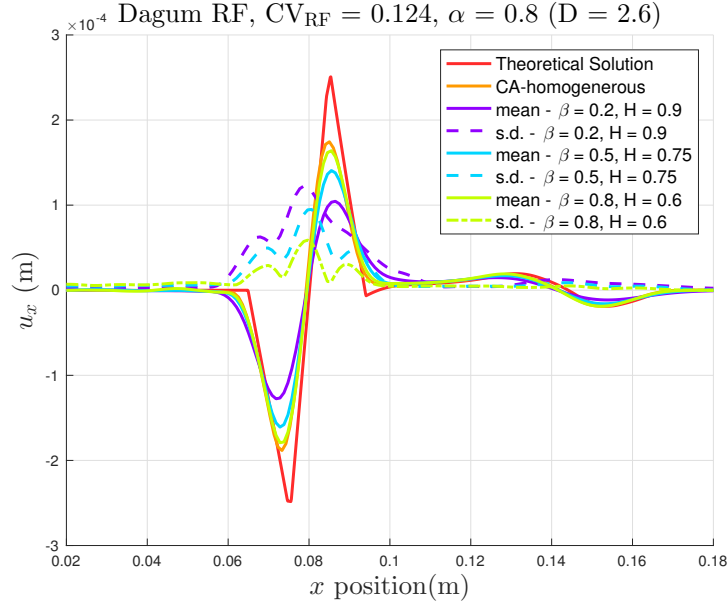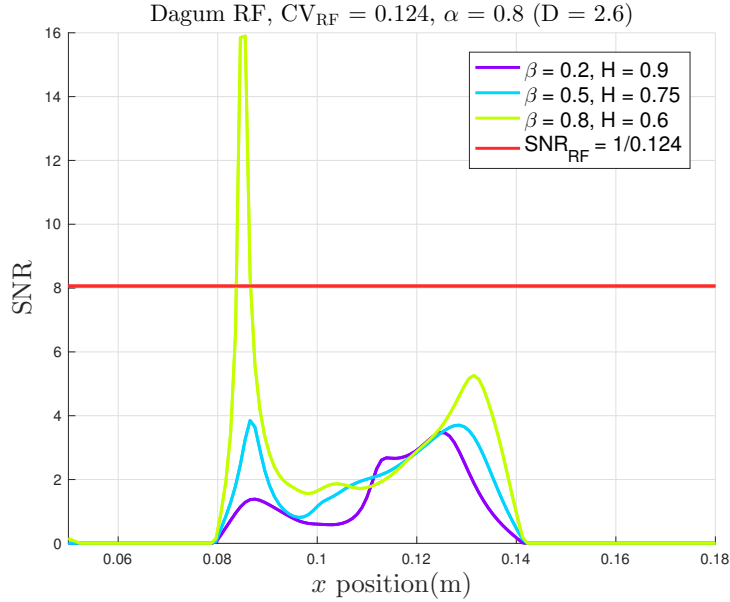
46

Figure 3.7: Cauchy RFs with $CV_{RF}= 0.124$: boundary for three different loading conditions of SNR_R and SNR_{RF} for varying α and β. (a) pressure wave, (b) Rayleigh wave. The boundary for in-plane tangential load between SNR_R less than or greater than SNR_{RF} is roughly represently by the green dotted line. The approximate boundaries for anti-plane shear load (the yellow line) and in-plane tangential load (the red line) are also indicated for comparison.

$(D = 2.6)$ and $\beta = 0.6, 0.75, 0.9$ are plotted separately and compared with homogeneous results and theoretical solution.

Figure 3.9 shows a comparison of SNR_R and SNR_{RF} for varying α and β for Dagum RFs for an applied pure moment, an in-plane tangential load, anti-plane shear force and in-plane normal load. Only when β is very small (less than 0.2), do we see SNR_R greater than SNR_{RF}, which suggests that, in general, the fluctuations of the response are smaller than the fluctuation of the underlying RFs. One more interesting aspect is that the Rayleigh wave changes faster than the pressure wave, as was found in the normal load case [33]. In general,

(a) Mean and s.d. of Dagum RFs

(b) SNR of response versus SNR of RF

Figure 3.8: Pure moment responses: Dagum RFs responses at $y = 0$ with $\alpha = 1.8$ (D = 2.1) and varying β. (a): mean and s.d. of random fields responses versus homogeneous medium results; (b) SNR of response versus SNR of RF.

the plots of Figure 3.9 are qualitatively the same and quantitatively very similar to those of [33].
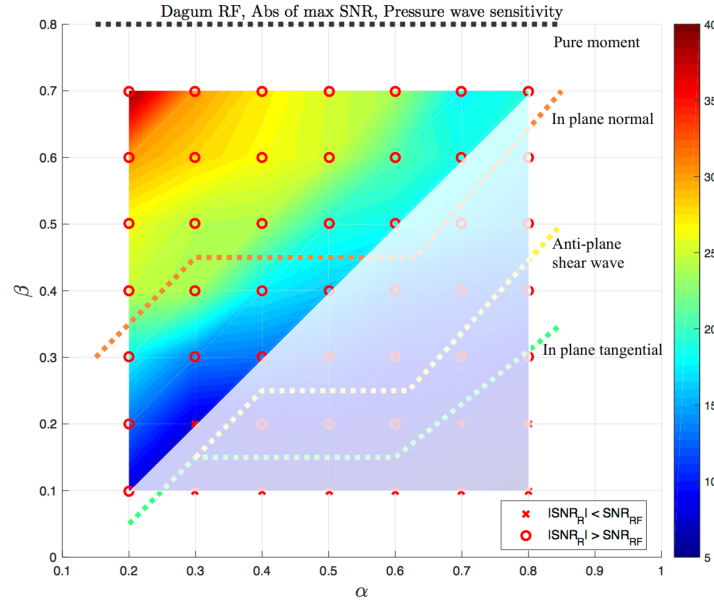
(a) Dagum: SNR for Pressure Wave
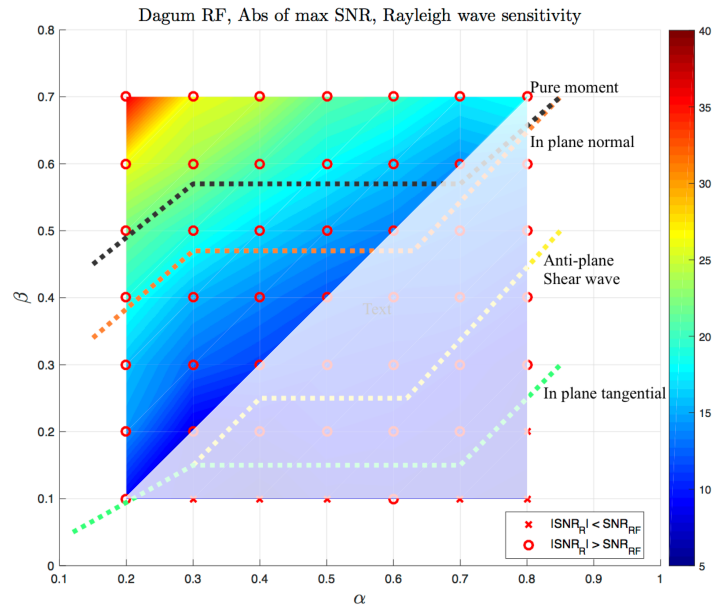
(b) Dagum: SNR for Rayleigh Wave

Figure 3.9: Dagum RFs with CV_{RF}= 0.124: boundary for three different loading condition of SNR_R and SNR_{RF} for varying α and β. (a) Pressure wave, (b) Rayleigh wave. The boundary for in-plane tangential load between SNR_R less than or greater than SNR_{RF} is roughly represently by the green dotted line. The approximate boundaries for anti-plane shear load (the yellow line) and in-plane tangential load (the red line) are also indicated for comparison.

3.5 Summary [2]

This chapter reports the dynamic responses of Lamb-type problems where concentrated tangential force and moment are applied to a half-space in plane strain (effectively, half-plane) with random mass density field with fractal and Hurst characteristics separately. Both features are decoupled here by employing Cauchy and Dagum RF models which do not any self-affinity. The cellular automata is used to simulate, in a Monte Carlo sense, the transient wave propagation as it allows assignment of random heterogeneous material properties on the cell level. The sensitivity of the response is then studied with a comprehensive evaluation for fractal dimension and Hurst effects for both loading cases.

In general, we find the response to be more sensitive to the Hurst parameter (H) than to the fractal dimension (d) of the mass density RF for all the loading scenarios. Only when β is small enough (less than 0.2) for both Cauchy and Dagum RFs, is the fluctuation of the response very significant. In general, for the same random field, the Rayleigh wave changes faster than the pressure wave with respect to the same varying parameters. Compared with responses corresponding to the normal load on the same RFs [10], we find the responses under tangential load to be less sensitive to both fractal and Hurst effects, while the responses under the concentrated moment are more sensitive to both fractal and Hurst effects compared with all other loading cases. I have also included the comments section in our recent paper.

3.5.1 Comments on the deterministic field and the average field

The foregoing effect of wave scattering and amplitude loss would also occur in the case of elastodynamics of a medium of random (or even constant) mass density and spatially random stiffness tensor. In principle, both quantities are random and their determination of needs to be done for specific materials.

Altogether, the discussion containing (1.1)-(1.5) can be applied to posing the elastodynamics

---

[2]The comments of this section are taken out from Ostoja-Starzewski's work in [65].

in terms of the stress field [37], which is a much less known (albeit advantageous in various situations) procedure than the 150-year old displacement formulation (involving the Navier equation, etc.). Then, (1.1) would be interpreted as the Ignaczak equation for the stress field.

Finally, one can also interpret (1.1) as a field equation of any mechanics/physics phenomenon, involving an integral-differential operator, the key thing being that the solution of (1.5) is generally different from a solution of (1.4). Which inequality (either < or >) will come out one cannot say in advance, but one generally knows that there will be an inequality between both types of solutions, i.e. between a correct solution to a stochastic problem and a deterministic solution to a straightforwardly averaged one.

3.5.2   Comments on fractional calculus

A very interesting issue is the interplay of fractals with fractional calculus, both in the time and space domains. An often-cited application is a viscoelasticity, where fractional temporal derivatives provide a compact constitutive model. However, finding a definite link between a spatially fractal structure of a viscoelastic material and its postulated fractional model remains an outstanding challenge [39]. The last few decades have seen much activity in partial differential equations (PDEs) where temporal and/or spatial derivatives are assumed to be fractional. The article [22] discusses the formulation of a continuum mechanics model smoothing a fractal porous microstructure. Here we note that there exists no solution to a Lamb-type problem with space fractional derivatives, which would directly correspond to (at least) the anti-plane elastodynamics problem in random, linear elastic medium [64]. The closest model relative to the focus of our paper is a diffusion-wave equation with constant coefficients in [44]. In view of the above-mentioned weak dependence of the diffusion equation on spatial randomness, we do not pursue this topic here.

Chapter 4

Anti-plane shear Lamb's problem on tensor random fields (TRF)[1]

In a series of aforementioned studies, we investigated the anti-plane and in-plane Lamb wave propagations in media with random fields of mass density and spatially homogeneous isotropic linear elasticity [34,64,65]. In order to consider the overall spatial randomness, we then extend these studies to include such randomness also in the anti-plane stiffness tensor, while admitting its full anisotropy, i.e. not forcing it to be locally isotropic.

To model the spatial statistics of the anti-plane stiffness tensor with full anisotropy, we work with a second-rank tensor random field (TRF) [25,26,63]. This is done by taking the dyadic product of two scalar random fields generated from Cauchy or Dagum correlation functions, the details are presented in Chapter 1.

Overall, this chapter is organized as follows. Section 4.1 presents the general cellular automata for auti-plane shear Lamb's problem with a random anti-plane stiffness tensor. Section 4.2 presents Cauchy and Dagum RFs results and provides a comprehensive comparison with just a random mass density field or with a locally isotropic stiffness tensor. Finally, Section 4.3 provides some concluding remarks about this chapter.

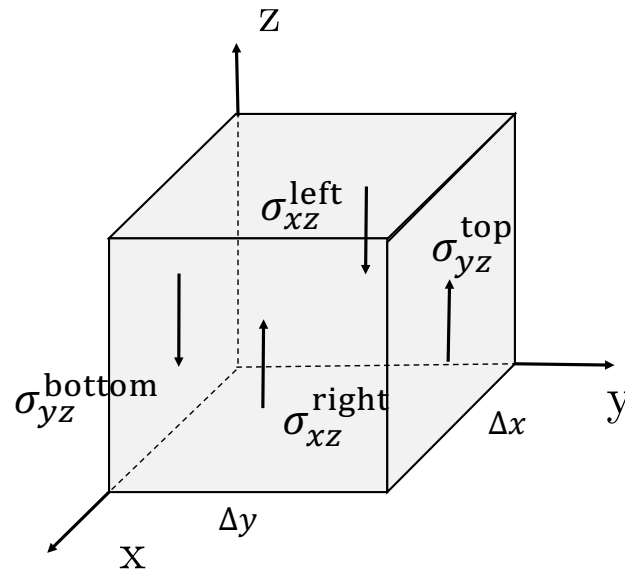## 4.1   Cellular automata for anti-plane with stiffness tensor random field

This section aims to detail the CA approach for anti-plane shear problem while we introduce randomness into stiffness tensor. The numerical method is presented in terms of shear force,

---

[1]The content of this chapter is mostly taken out from our work in [65].

balance of momentum, stepping algorithm and boundary condition.
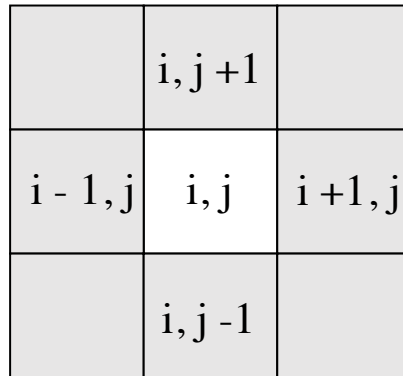
(a) cell (i,j) of CA

(b) Neighbor stresses on cell(i,j)

Figure 4.1: (a) cell (i,j) and its neighbors for Cellular Automata discretization (b) the neighbor stresses acting on cell (i,j).

In CA, the state of each cell depends on the cells that share an edge with this cell. For anti-plane problem, a cell state is defined by its displacement, velocity and external force. The only non-zero components are in the z direction: displacement u_z, velocity v_z, and external force F_z. All of those quantities are functions of x and y. Analogous to the in-plane development in [20], after introducing randomness, we have the formulations for the shear

forces calculated for the cell (i, j)

$$
\begin{aligned}
F_z^{top} &= (w\Delta x)\sigma_{yz}^{top} \\
&= (w\Delta x)\frac{^{i,j+1}\mu_{22} +_{i,j} \mu_{22}}{2}\frac{^{i,j+1}u_z -_{i,j} u_z}{\Delta y} \\
&+ (w\Delta x)\frac{^{i+1,j}\mu_{12} +_{i,j} \mu_{12}}{2}\frac{^{i+1,j}u_z -_{i,j} u_z}{\Delta x}
\end{aligned}
\tag{4.1a}
$$

$$
\begin{aligned}
F_z^{bottom} &= (w\Delta x)\sigma_{yz}^{bottom} \\
&= (w\Delta x)\frac{^{i,j}\mu_{22} +_{i,j-1} \mu_{22}}{2}\frac{^{i,j}u_z -_{i,j-1} u_z}{\Delta y} \\
&+ (w\Delta x)\frac{^{i,j}\mu_{12} +_{i-1,j} \mu_{12}}{2}\frac{^{i,j}u_z -_{i-1,j} u_z}{\Delta x}
\end{aligned}
\tag{4.1b}
$$

$$
\begin{aligned}
F_z^{right} &= (w\Delta y)\sigma_{xz}^{right} \\
&= (w\Delta y)\frac{^{i+1,j}\mu_{11} +_{i,j} \mu_{11}}{2}\frac{^{i+1,j}u_z -_{i,j} u_z}{\Delta x} \\
&+ (w\Delta y)\frac{^{i,j+1}\mu_{12} +_{i,j} \mu_{12}}{2}\frac{^{i,j+1}u_z -_{i,j} u_z}{\Delta y}
\end{aligned}
\tag{4.1c}
$$

$$
\begin{aligned}
F_z^{left} &= (w\Delta y)\sigma_{xz}^{left} \\
&= (w\Delta y)\frac{^{i,j}\mu_{11} +_{i-1,j} \mu_{11}}{2}\frac{^{i,j}u_z -_{i-1,j} u_z}{\Delta x} \\
&+ (w\Delta y)\frac{^{i,j}\mu_{12} +_{i,j-1} \mu_{12}}{2}\frac{^{i,j}u_z -_{i,j-1} u_z}{\Delta y}
\end{aligned}
\tag{4.1d}
$$

where w is the width in the z direction, and Δx and Δy are cell spacings in x, y directions, respectively.

With an external loading F_z^{ext}, The balance of momentum, see Figure 4.1(b) for the cell (i, j) gives

$$
\rho w\Delta x\Delta y\dot{v}_z = F_z^{ext} + (F_z^{right} + F_z^{top} - F_z^{left} - F_z^{bottom}),
\tag{4.2}
$$

where $\dot{v}_z$ is the time derivative of v_z. Similar to the in-plane problem [20], we introduce an integer m representing the number of steps per second, so that, for each time step, we can

update the velocity at $(k + 1)$st step based on the kth step as

$$v_z^{k+1} = v_z^k + \frac{\dot{v_z}}{m}. \tag{4.3}$$

The displacement is updated correspondingly as

$$u_z^{k+1} = u_z^k + \frac{1}{m}v_z^{k+1}. \tag{4.4}$$

Finally, the CA requires two common boundary conditions. The free surface is modeled by adding an additional layer of cells, for which the stresses on the matching face are enforced to be zero. The displacement and velocity boundary conditions can be prescribed directly. For the anti-plane shear problem, the free surface condition is $_{i,1}\sigma_{yz}^{bottom} = 0$. The time stepping algorithm can be found in Table 2.1.

4.2 Random fields results and discussion

This section shows the results of the CA solutions for both Cauchy and Dagum RFs. Study in [64,65] has reported the convergence of the CA solution with increasing mesh refinement on both homogeneous media and random media with white noise. The results for only random mass density field for both Cauchy and Dagum RFs were also reported in [64]. This section reports and compares the following dynamic cases: (1) only introducing randomness into mass density field and the shear modulus remains deterministicly constant; (2) introduce randomness into mass density and randomness into shear stiffness tensor with the assumption of local isotropy; (3) the combination of a random mass scalar field and an inhomogeneous second-rank tensor field with full anisotropy. We focus on the average dynamic responses and the fluctuations of displacements for all cases.

4.2.1 Cauchy random field responses

This section focuses on the dynamic surface displacements in the x-direction for Cauchy RFs of the aforementioned three cases. Figure 4.2 firstly visualizes the three components of one realization of Cauchy random stiffness tensor fields $C(\omega, \mathbf{x})$ with $\alpha = 1.8$ and $\beta = 0.2$. The sum of the diagonal terms C_{11} and C_{22} have the same signal to noise as mass density field introduced in Chapter 2. The off-diagonal terms C_{12} is obtained by taking the dyadic product of two scalar random fields d_1 and d_2 generated by the Cauchy or Dagum correlation functions defined in Section 1.2.1.
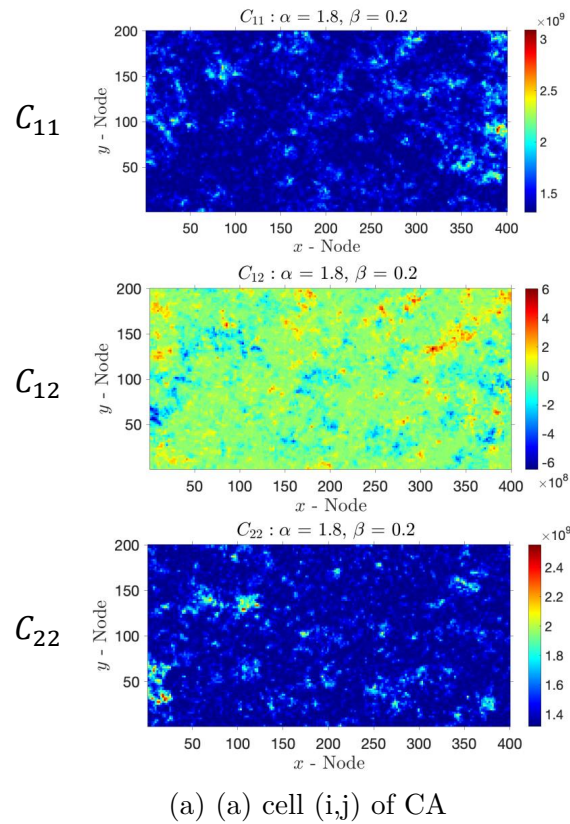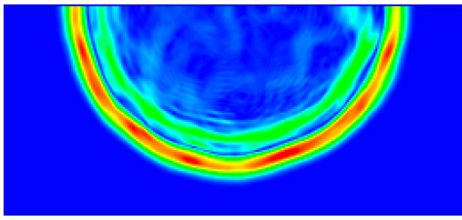

(a) (a) cell (i,j) of CA

Figure 4.2: Visualization of the components of one realization of Cauchy random anti-plane stiffness tensor fields with $\alpha = 1.8$ and $\beta = 0.2$.
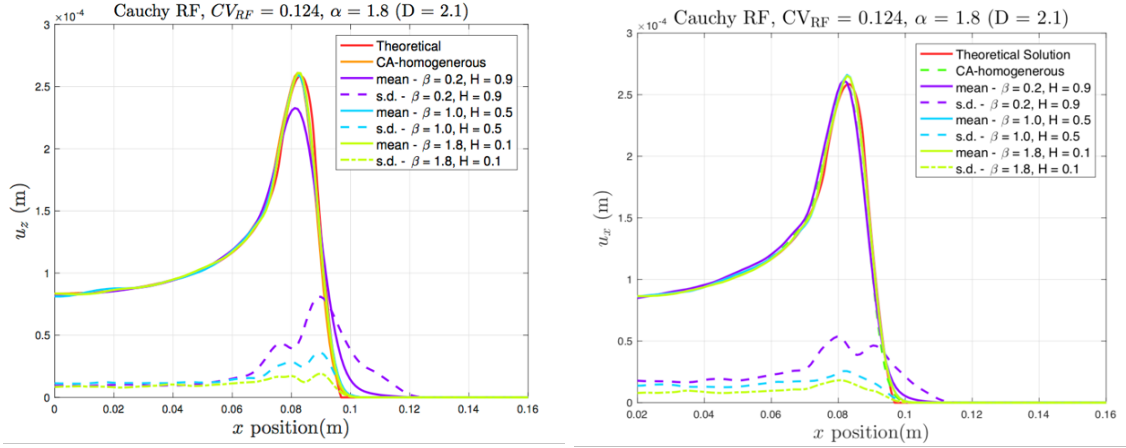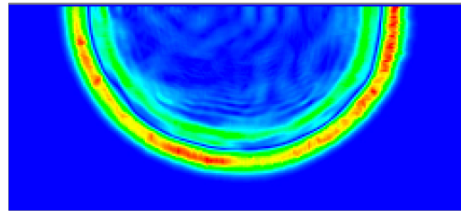
(a) Random ρ and const C

(b) Constρ and random C
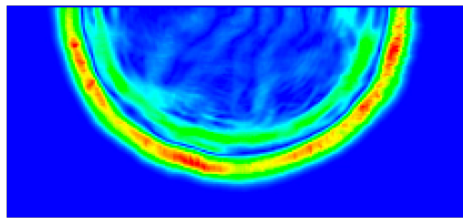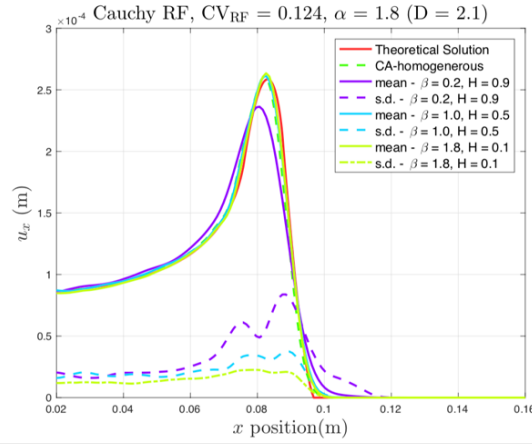
(c) Random ρ and C

Figure 4.3: Cauchy RFs surface responses with $\alpha = 1.8$ ($D = 2.1$) and varying β for three cases. top: mean and standard deviation (s.d.) of random fields responses versus the theoretical and homogeneous field results; bottom: von Mises stress profile on a mesh set at $N_x = 1024$ up to the time 92 μs.
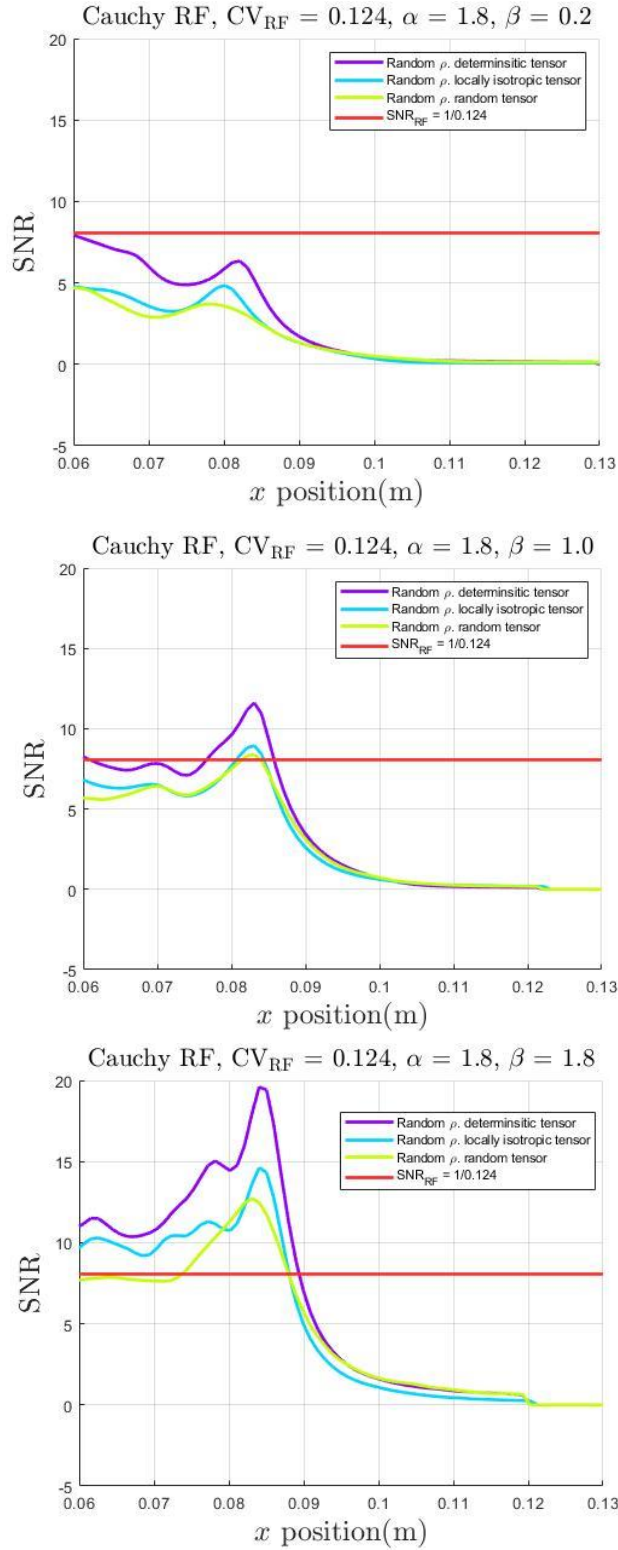
Figure 4.4: Comparisons of different random field models on SNR of response versus SNR of RF. (a) SNR comparison of three cases for $\alpha = 1.8$ and $\beta = 0.2$; (a) SNR comparison of three cases for $\alpha = 1.8$ and $\beta = 1.0$;(a) SNR comparison of three cases for $\alpha = 1.8$ and $\beta = 1.8$

Figure 4.5: Cauchy RFs with $CV_{RF}= 0.124$: boundary for second-rank tensor model with full anisotropy of SNR_R and SNR_{RF} for varying α and β. The boundary for anti-plane load between SNR_R less than or greater than SNR_{RF} is roughly represented by the orange dotted line.

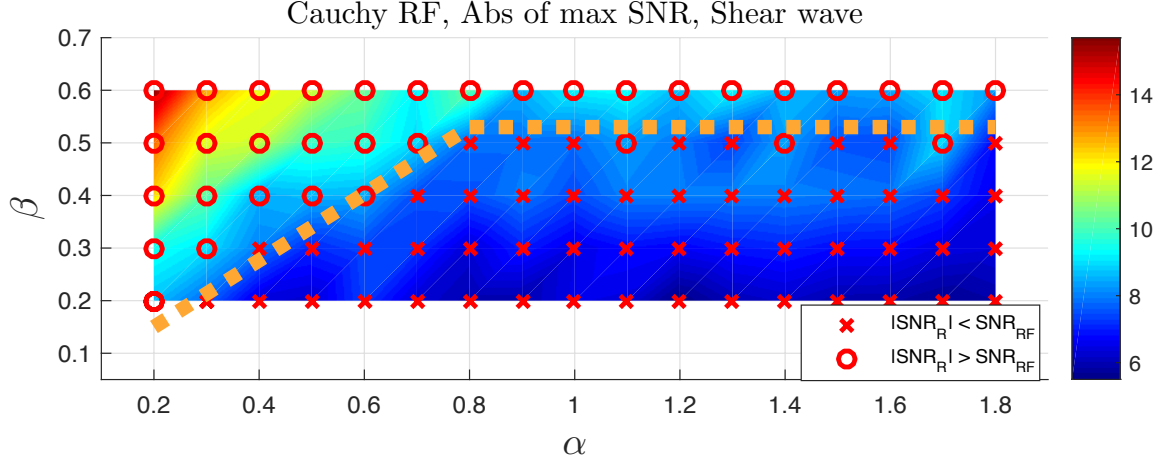We consider the displacement and stress responses up to the time 92μs. Figure 4.3 shows the displacement and stress responses of an applied shear load with RFs with $\alpha = 1.8$ ($D = 2.1$) and three values of β. For all three cases, the mean and standard deviation of 128 realizations with $\alpha = 1.8$ ($D = 2.1$) and $\beta = 0.2, 1.0, 1.8$ are plotted separately and are compared with the homogeneous results and theoretical solution. As β increases, the mean becomes closer to the homogeneous results and the standard deviation decreases. The Hurst parameter continues to have a stronger effect on the responses than the fractal dimension for both the random mass density field and the tensor random field. Additionally, the von Mises stress profiles on one realization from each case are also plotted in Figure 4.3.

Figure 4.5 compares SNR_R and SNR_{RF} for a second-rank tensor model with full anisotropy for varying α and β. Only when β is greater than 0.5 and α is smaller than 0.4 , do we see SNR_R greater than SNR_{RF}, which suggests that, in general, the fluctuations of the response are larger than the fluctuation of the underlying RFs. In general, the plots of Figure 4.5 are qualitatively the same and quantitatively very similar to those reported in [64, 65].

To have a better understanding about the comparisons over the whole α and β plane , Figure 4.6 shows the SNR plane for all three cases. Case 1 which only has a random mass density field with a homogeneous, isotropic tensor field has the largest SNR, which represent
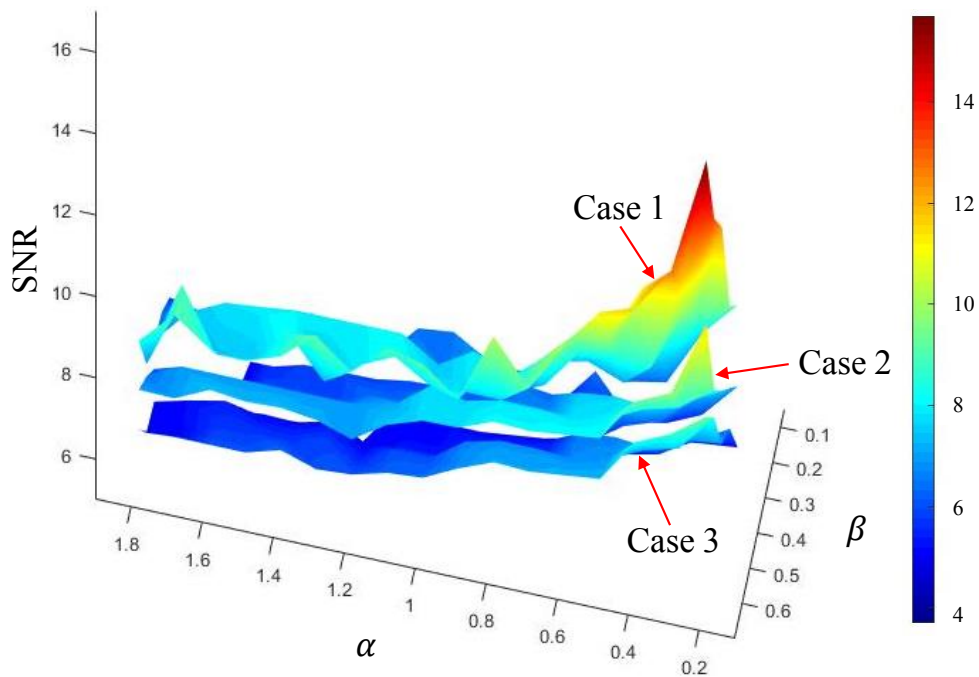
Figure 4.6: Cauchy RFs: SNR plane for all three cases Cauchy RFs where $\alpha \in [0.2, 1.8]$ and $\beta \in [0.2, 0.6]$. Case 1: only random mass density field and a homogeneous stiffness tensor; Case 2: a random mass density field and an inhomogeneous stiffness tensor with local isotropy; case 3: random mass density field with a second-rank tensor model with full anisotropy.

the smallest fluctuation of the displacement responses. Just like Cauchy RFs, a second-rank tensor model with full anisotropy is also more sensitive than locally isotropic random tensor for all α and β combinations.

4.2.2 Dagum random field response

This section reports the surface displacement responses and their spatial sensitivity for Dagum RFs of the three cases.
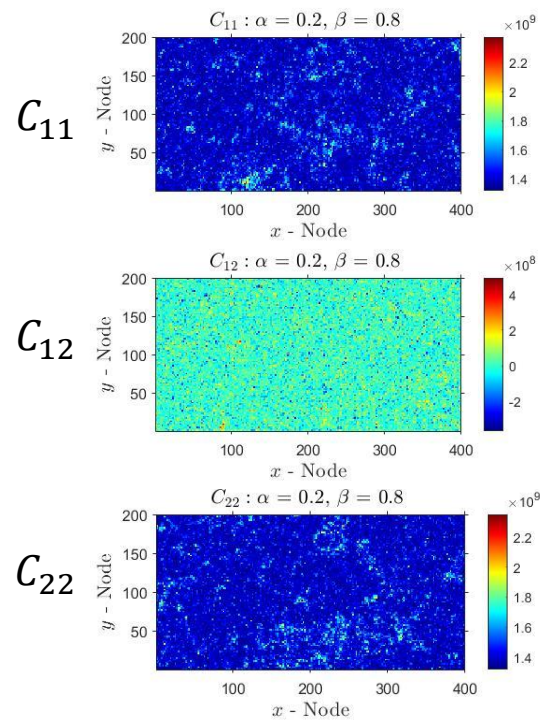
(a) (a) cell (i,j) of CA

Figure 4.7: (a) Visualization of the components of 1 realization of Dagum random stiffness tensor fields with $\alpha = 0.2$ and $\beta = 0.8$.
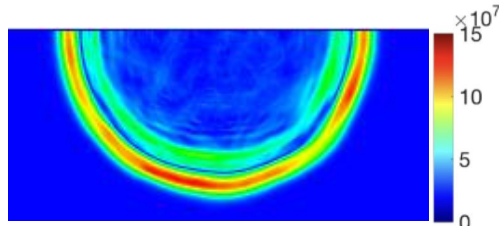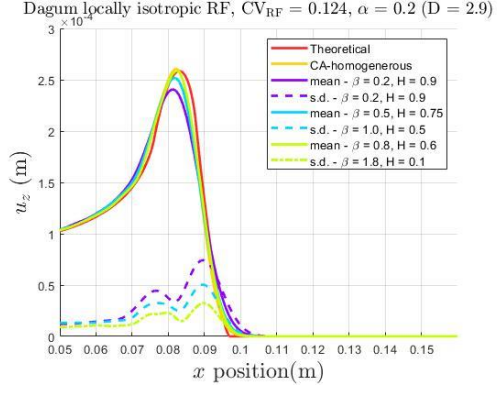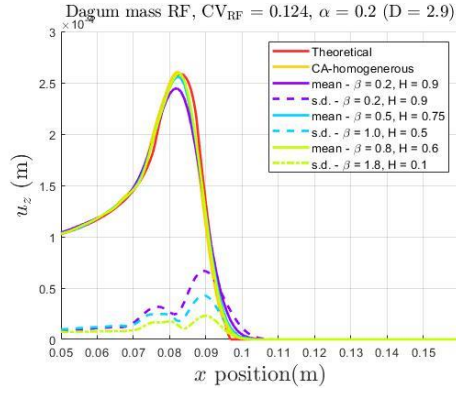
von Mises Stress Profile for one
realization at $\alpha = 0.2, \beta = 0.2$

(a) Random ρ and const C
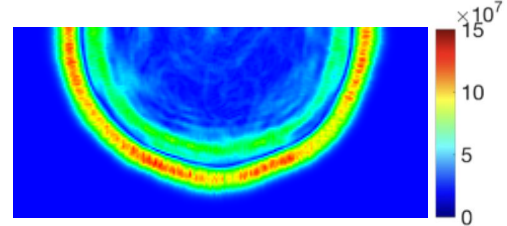
von Mises Stress Profile for one
realization at $\alpha = 0.2, \beta = 0.2$

(b) Constρ and random C
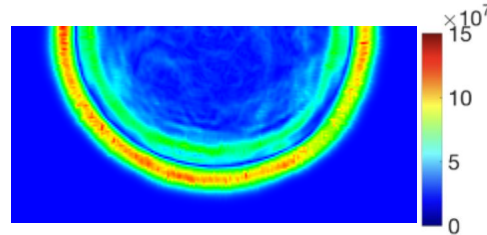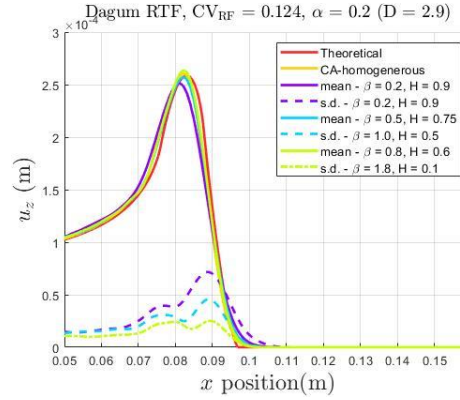
von Mises Stress Profile for one
realization at $\alpha = 0.2, \beta = 0.2$

(c) Random ρ and C

Figure 4.8: Dagum RFs surface responses with $\alpha = 1.8$ ($D = 2.1$) and varying β for three cases. top: mean and standard deviation (s.d.) of random fields responses versus the theoretical and homogeneous field results; bottom: von Mises stress profile on a mesh set at $N_x = 1024$ up to the time 92 μs.

62
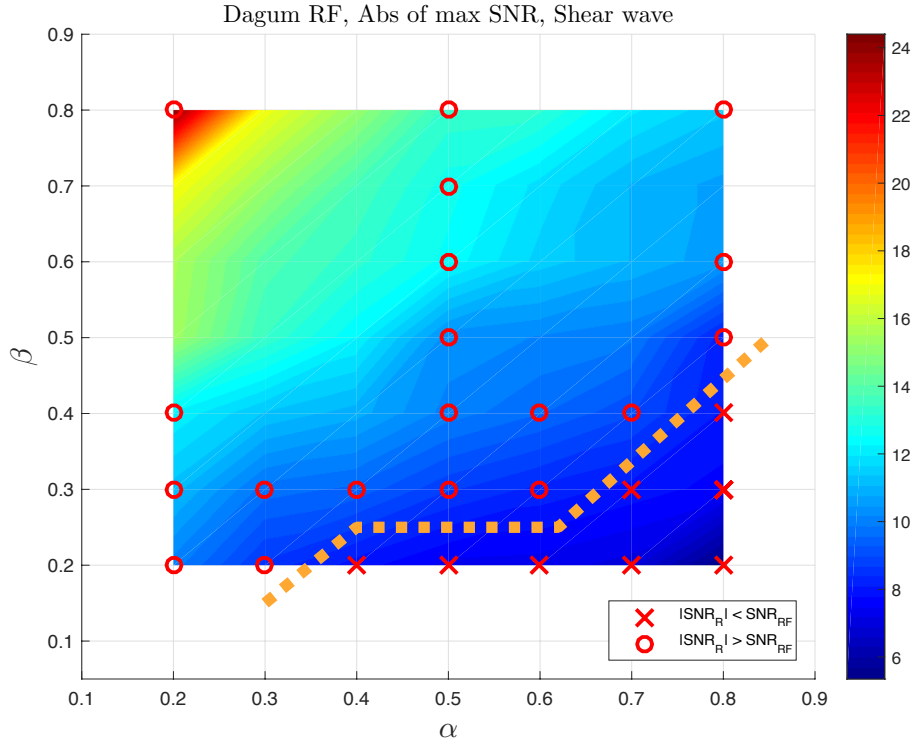
Figure 4.9: Dagum RFs with $CV_{RF} = 0.124$: boundary for second-rank tensor model with full anisotropy of SNR_R and SNR_{RF} for varying α and β. The boundary for anti-plane load between SNR_R less than or greater than SNR_{RF} is roughly represented by the orange dotted line
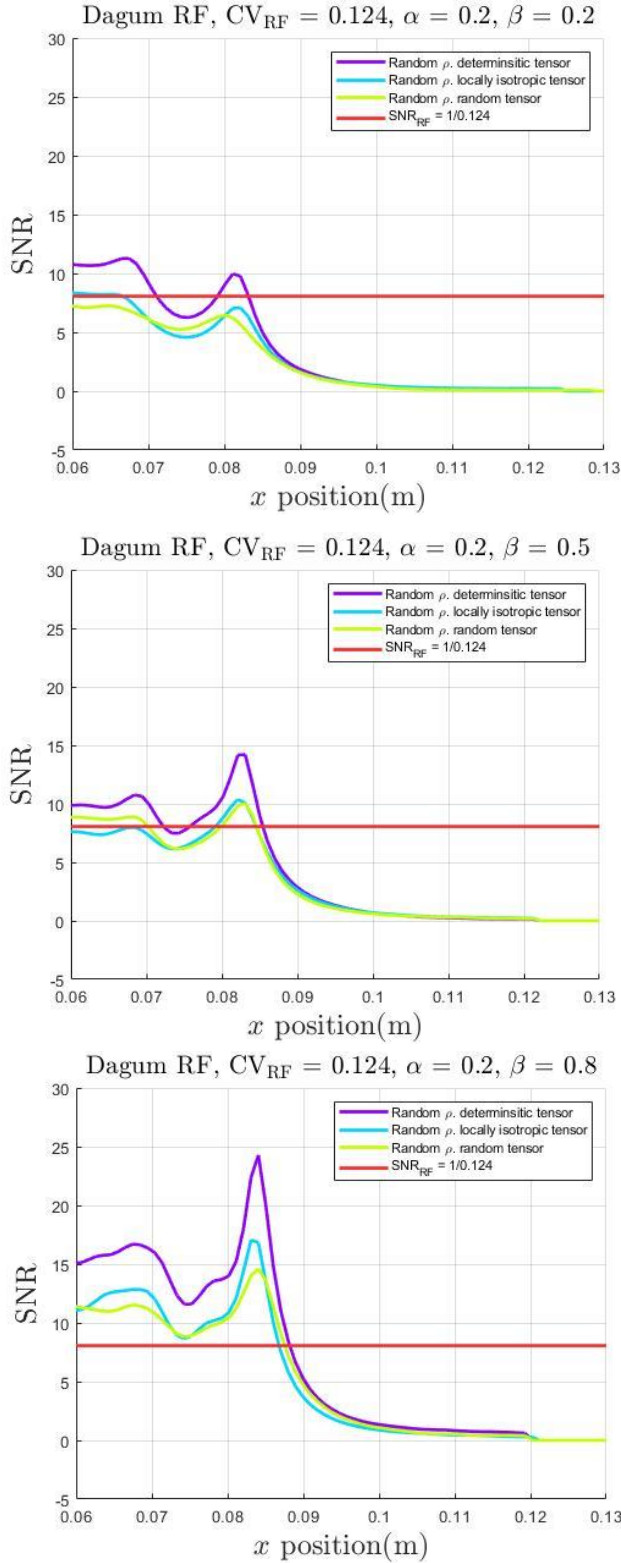
Figure 4.10: Comparisons of different random field models on SNR of response versus SNR of RF. (a) SNR comparison of three cases for $\alpha = 1.8$ and $\beta = 0.2$; (a) SNR comparison of three cases for $\alpha = 1.8$ and $\beta = 1.0$;(a) SNR comparison of three cases for $\alpha = 1.8$ and $\beta = 1.8$

64
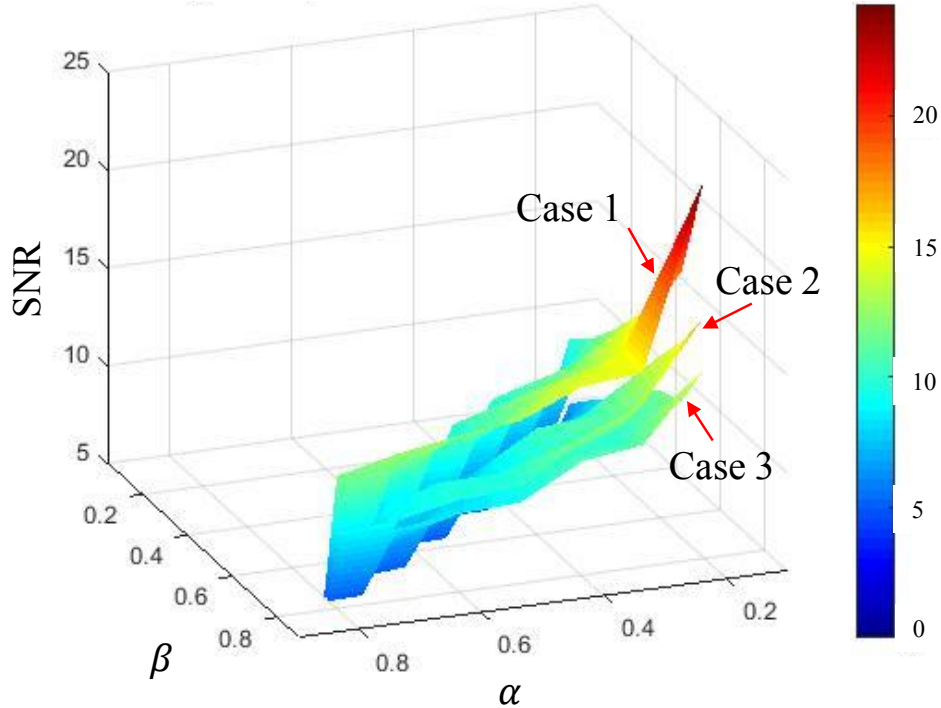
Figure 4.11: Dagum RFs: SNR plane for all three cases Cauchy RFs where $\alpha \in [0.2, 0.8]$ and $\beta \in [0.2, 0.8]$. Case 1: only random mass density field and a homogeneous stiffness tensor; Case 2: a random mass density field and a inhomogeneous stiffness tensor with local isotropy; case 3: random mass density field with a second-rank tensor model with full anisotropy.

Figure 4.7 again visualizes the three components of one realization of Dagum random stiffness tensor fields $\boldsymbol{C}(\omega, \mathbf{x})$ with $\alpha = 0.2$ and $\beta = 0.8$. The sum of diagonal terms C_{11} and C_{22} have the same signal to noise ratio as mass density field. The off-diagonal terms C_{12} is obtained by taking the dyadic product of two rscalar random field d_1 and d_2 generated using the Dagum correlation (covariance) functions.

Figure 4.8 shows the displacement and stress responses of an applied shear load with RFs with $\alpha = 1.8$ ($D = 2.1$) and three values of βs. For all three cases, the mean and standard deviation of 128 realizations with $\alpha = 0.2$ ($D = 2.9$) and $\beta = 0.2, 0.5, 0.8$ are plotted separately and are compared with the homogeneous results and theoretical solution. Similar to Cauchy RFs, as β increases, the mean becomes closer to the homogeneous results and the standard deviation decreases. Additionally, von Mises stress profiles on one realization from

each fractal and Hurst combination are also plotted in Figure 4.3.

To study the sensitivity of responses for a second-rank tensor model with full anisotropy, Figure 4.9 presents the comparison of SNR_R and SNR_{RF} for varying α and β. Only when β greater than 0.4 and α smaller than 0.5 , do we see SNR_R greater than SNR_{RF}, which suggests that, in general, the fluctuations of the response are larger than the fluctuation of the underlying RFs. In general, the plots of Figure 4.5 show that after we introduce randomness into the mechanical properties, the fluctuation for the responses becomes larger compared with those of [64, 65].

To compare the spatial sensitivity of a second-rank tensor model with full anisotropy with a deterministic mechanical property field and a locally isotropic tensor random field, we plotted comparisons of those three cases on SNR of response versus SNR of RF in Figure 4.10. The left figure is a comparison for Dagum RF with $\alpha = 0.2$ and $\beta = 0.2$, the inhomogeneous second-rank tensor model with full anisotropy has the smallest SNR, thus biggest fluctuation, which is followed by case 2 an inhomogeneous tensor model with the assumption of local isotropy. Case 1 with only random mass density field has the largest SNR, thus the smallest fluctuation. We plotted the comparison for $\beta = 0.5$ and $\beta = 0.8$ for the same α and for all the cases, a second-rank tensor model with full anisotropy is the most sensitive.

To have a better understanding about the comparisons over the whole α and β plane, Figure 4.11 shows the SNR plane for all three cases. Case 1 which only has a random mass density field with a homogeneous, isotropic tensor field has the largest SNR, which represent the smallest fluctuation of the displacement responses. Just like Cauchy RFs, a second-rank tensor model with full anisotropy is also more sensitive than locally isotropic tensor random fields for all α and β combinations.

4.3   Summary

Whereas numerous studies of wave propagation in random media were reported in literature, they were typically set in locally isotropic media, i.e. those modeled by scalar-valued RFs with very simple correlation structures. The few studies that did admit local anisotropy of the elasticity tensor were restricted to white-noise correlations or only one term of the correlation function representation. The present study is the first in SPDEs to admit tensor-valued random fields of elastic anisotropic properties having very rich correlations: fractal and long-range spatial memory.

The paper investigates the combined effects of spatial randomness in both mass density and anti-plane stiffness tensor fields for Lamb-type problems. The randomness is introduced with fractal and Hurst characteristics, like many patterns found in nature. Both fractal and Hurst effects are decoupled here by employing Cauchy and Dagum RF models which do not presuppose any self-affinity. The randomness in mechanical property is introduced by a second-rank tensor model with full anisotropy. The cellular automata is used to simulate, in a Monte Carlo sense, the transient wave propagation as it allows assignment of random heterogeneous material properties on the cell level. The sensitivity of the response is then studied with a comprehensive evaluation of fractal dimension and Hurst effects. The results are compared with those for the model having the random mass density field and the tensor random field model with local isotropy.

In general, we find the response to be more sensitive to the Hurst parameter (H) than to the fractal dimension (d) for all random field models. When β is greater than 0.5 and α is smaller than 0.4 for both Cauchy and Dagum RFs, the combined fluctuation effects of the displacement response are very significant. A second-rank tensor model with full anisotropy has the strongest sensitivity, followed by a locally isotropic tensor random model for all α and β combinations.

Chapter 5

Summary and conclusion

5.1 Summary

This thesis has developed an integrative framework that tightly connects the random field modeling, cellular automata numerical solver to analyze force and moment problems in random media with fractal and Hurst effects. We introduced randomness into both mass density field and stiffness tensor field. For the scalar mass density random field, we work with second-order, wide-sense stationary and isotropic models generated from Cauchy or Dagum covariance functions. Cauchy and Dagum RFs can capture and decouple the fractal and Hurst effects. For the stiffness tensor random field, we adopt a newly proposed model with consideration of full anisotropy by taking the dyadic product of two scalar random fields generated from Cauchy or Dagum correlation functions. Since there exist no closed solution for transient waves in random-fractal media, we resort to numerical investigations. A solver called cellular automata (CA) is developed and implemented to simulate the dynamical responses for both anti-plane and in-plane Lamb's problems. The developed solver is verified on homogoneous media and random media with white noise by benckmarking with classical theoretical solutions. Through a comprehensive study for both Cauchy and Dagum random field models, the sensitivity of wave propagation under different loadings is assessed for a wide range of fractal and Hurst parameters. We find out that for some range of fractal and Hurst parameters, the effective medium wave equations can not work for transient wave problems in random media.

In Chapter 2, we formulate and implement the cellular automata (CA) to simulate the anti-

plane shear wave propagation in random media. Both Cauchy and Dagum random field models are used to capture fractal dimension and Hurst effects in mass density field. We first evaluate the dynamic responses of random mass density by comparing them with the homogenerous computational results and the classical theoretical solution. Then a comprehensive study is carried out for different combinations of fractal and Hurst coefficients. We study the spatial imperfection senstivity and determine to what extent fractal and Hurst effects are significant enough to change the dynamic responses by comparing the the signal-to-noise ratio of the response versus the signal-to-noise ratio of the introduced random mass density field.

In Chapter 3, we generalize our numerical solver to half-space in plane wave propagations with the same random mass density field with fractal and Hurst characteristics. Cellular automata (CA) is firstly reframed and verified on progressively refined meshes of both homegeneous medium and random medium with white noise. A comprehensive study is for different combinations of fractal and Hurst coefficients is then conducted and the results show that for all loading cases, displacement responses are more sensitive to Hurst effects than fractal dimension. Pressure wave and Rayleigh wave responses are also investigated and compared both qualitatively and quantitatively. Rayleigh wave is found to be more sensitive than pressure wave under the same mass random field and loading.

In Chapter 4, we introduce fractal and Hurst effects to a second-rank anti-plane stiffness tensor random field (TRF) model with full anisotropy. We then generalize the cellular automata solver to incorporate the spatial randomness both in mass density as well as the stiffness tensor fields. A comprehensive sensitivity comparion study for anti-plane Lamb's problem is conducted among three stiffness tensor models: (1) a deterministic stiffness tensor; (2) a locally isotropic stiffness tensor with heterogeneity; (3) a second-rank tensor admitting full anisotropy and heterogeneity. The simulation results show that the fluctuation of displacement reponses on model (3) is the strongest, followed by model (2).

5.2 Future work

The progress made in this thesis can serve as a starting point for future stochastic mechanics research. Here we list a few possible research directions:

- The cellular automata numerical solver developed in this thesis is likely to open up possibilities to obtain solution for parabolic partial differential equations over a 2d domain $X \in \mathbb{R}^2$:

$$\nabla^2 \mathrm{T} + P(\mathbf{x}, t) = \frac{K}{\rho(\omega, \mathbf{x})C} \frac{\partial T}{\partial t}, \quad \mathbf{x} \in X \tag{5.1}$$

  which can describe 2D heat transfer, particle diffusion and dynamic pricing in financial market. Depending on the application, $P(\mathbf{x}, t)$ can represent the control input or a disturbance. The same numerical scheme can also be used to obtain the responses for elliptic equation with spatial randomenss:

$$\nabla \cdot (\boldsymbol{C}(\omega, \boldsymbol{x}) \nabla \boldsymbol{u}) = F(\boldsymbol{x}); \quad \mathbf{x} \in X \tag{5.2}$$

  where no time dependence is considered but often used to describe the equilibrium states. $F(\boldsymbol{x})$ represent a loading source. This work is currently under development in our research lab.

- The possible application of the random field models and numerical solver can be adopted for telegraph equation governed physics.

- This thesis has provided a general framework for sensitivity analysis when introducing randomness in the differential operator for stochastic wave propagation. But the solver and random field model can be generated to material random field models with different correlation functions or to incorporate randomness in the forcing and boundary conditions.

5.3 Conclusion

This dissertation focuses on the investigation of responses for transient wave propagation while admitting material spatial randomness into both a scalar mass density field and a tensor random field, both assumed to have fractal and Hurst effects. In general, this thesis has made contributions in areas of random field modeling, numerical scheme for elastodynamics and sensitivity analysis for wave propagations. Specifically, we adopt a mass random density field with fractal and Hurst effects and an anti-plane stiffness tensor model with full anisotropy by taking the dyadic product of two scalar RFs generated from Cauchy or Dagum correlation functions. We developed and implemented a generalized cellular automata numerical scheme that can incorporate the defined spatial randomness. Throughout this thesis, cellular automata are tested and validated for anti-plane and in-plane Lamb's problem and comprehensive sensitivity study are conducted on a wide range of fractal and Hurst effects. The synthesis process of incorporating spatial randomness into material properties are presented for both scalar and tensor random field. The cellular automata solver is presented in detail for each forcing problem in terms of force, balance of momentum, boundary condition and stepping algorithm. The fluctuations of shear wave, pressure wave and Rayleigh waves are evaluated both qualitatively and quantitatively for random mass density field. A senstivity study of anti-plane shear wave responses, on three different tensor models, is also conducted.

Looking ahead, advancement of parallel computing, efficient numerical solvers, together with the tensor random field framework adopted in this thesis have the potential to invesitgate the responses of dynamic and static systems in random media more efficiently.

Bibliography

[1] Jan D. Achenbach. *Wave Propagation in Elastic Solids*, volume 16. Elsevier, 2012.

[2] Bogdan F. Apostol. Elastic equilibrium of the half-space revisited. Mindlin and Boussinesq problems. *Journal of Elasticity*, 125(2):139–148, 2016.

[3] Michael Batty, Helen Couclelis, and Mark Eichen. Urban systems as cellular automata. *Environment and Planning*, 1997.

[4] Shikui Chen, Wei Chen, and Sanghoon Lee. Level set based robust shape and topology optimization under random field uncertainties. *Structural and Multidisciplinary Optimization*, 41(4):507–524, 2010.

[5] Bastien Chopard and Michel Droz. *Cellular Automata*, volume 1. Springer, 1998.

[6] George Christakos. *Random Field Models in Earth Sciences*. Courier Corporation, 2012.

[7] James W. Dally and Stephen A. Thau. Observations of stress wave propagation in a half-plane with boundary loading. *International Journal of Solids and Structures*, 3(3):293–300, IN1–IN5, 301–308, 1967.

[8] Tarik Faouzi, Emilio Porcu, Igor Kondrashuk, and Anatoliy Malyarenko. A deep look into the dagum family of isotropic covariance functions. *arXiv preprint arXiv:2106.14353*, 2021.

[9] Arthur Frankel and Robert W. Clayton. A finite-difference simulation of wave propagation in two-dimensional random media. *Bulletin of the Seismological Society of America*, 74(6):2167–2186, 1984.

[10] Tilmann Gneiting. Nonseparable, stationary covariance functions for space–time data. *Journal of the American Statistical Association*, 97(458):590–600, 2002.

[11] Tilmann Gneiting and Martin Schlather. Stochastic models that separate fractal dimension and the Hurst effect. *SIAM Review*, 46(2):269–282, 2004.

[12] István Gyöngy. Existence and uniqueness results for semilinear stochastic partial differential equations. *Stochastic Processes and their Applications*, 73(2):271–299, 1998.

[13] István Gyöngy. On stochastic finite difference schemes. *Stochastic Partial Differential Equations: Analysis and Computations*, 2:539–583, 2014.

[14] Takeyuki Hida and Si Si. *An Innovation Approach to Random Fields: Application of White Noise Theory*. World Scientific, 2004.

[15] Tran Duong Hien and Michał Kleiber. Stochastic finite element modelling in linear transient heat transfer. *Computer Methods in Applied Mechanics and Engineering*, 144(1-2):111–124, 1997.

[16] Alfons G. Hoekstra, Jiri Kroc, and Peter M. Sloot. *Simulating Complex Systems by Cellular Automata*. Springer, 2010.

[17] Ryan K. Hopman and Michael J. Leamy. Arbitrary geometry cellular automata for elastodynamics. *ASME International Mechanical Engineering Congress and Exposition*, 15:535–547, 11 2009.

[18] Eduardo Kausel. *Fundamental Solutions in Elastodynamics: A Compendium*. Cambridge University Press, 2006.

[19] Rossella Laudani, Dansong Zhang, Tarik Faouzi, Emilio Porcu, Martin Ostoja-Starzewski, and Leonardo P. Chamorro. On streamwise velocity spectra models with fractal and long-memory effects. *Physics of Fluids*, 33(3):035116, 2021.

[20] Michael J. Leamy. Application of cellular automata modeling to seismic elastodynamics. *International Journal of Solids and Structures*, 45(17):4835–4849, 2008.

[21] Michael J. Leamy and Adam C. Springer. Parallel implementation of triangular cellular automata for computing two-dimensional elastodynamic response on arbitrary domains. *International Conference on Vibration Problems*, pages 731–736, 2011.

[22] Jun Li and Martin Ostoja-Starzewski. Thermo-poromechanics of fractal media. *Philosophical Transactions of the Royal Society A*, 378(2172):20190288, 2020.

[23] Ming Li, Chuchu Chen, and Peijun Li. Inverse random source scattering for the helmholtz equation in inhomogeneous media. *Inverse Problems*, 34(1):015003, 2017.

[24] Xia Li and Anthony Gar-On Yeh. Neural-network-based cellular automata for simulating multiple land use changes using GIS. *International Journal of Geographical Information Science*, 16(4):323–343, 2002.

[25] Anatoliy Malyarenko and Martin Ostoja-Starzewski. Random fields related to the symmetry classes of second-order symmetric tensors. *International Conference on Stochastic Processes and Algebraic Structures*, pages 173–185, 2017.

[26] Anatoliy Malyarenko and Martin Ostoja-Starzewski. *Tensor-Valued Random Fields for Continuum Physics*. Cambridge University Press, 2019.

[27] Benoit B. Mandelbrot. *The Fractal Geometry of Nature*. WH Freeman New York, 1983.

[28] Benoit B. Mandelbrot and John W. Van Ness. Fractional brownian motions, fractional noises and applications. *SIAM Review*, 10(4):422–437, 1968.

[29] George D. Manolis and Christos Z. Karakostas. A green's function method to sh-wave motion in a random continuum. *Engineering Analysis with Boundary Elements*, 27(2):93–100, 2003.

[30] Bertil Matérn. *Spatial Variation*, volume 36. Springer Science & Business Media, 2013.

[31] Jorge Mateu, Emilio Porcu, and Orietta Nicolis. A note on decoupling of local and global behaviours for the Dagum random field. *Probabilistic Engineering Mechanics*, 22(4):320–329, 2007.

[32] Vinesh V. Nishawala and Martin Ostoja-Starzewski. Acceleration waves on random fields with fractal and Hurst effects. *Wave Motion*, 74:134–150, 2017.

[33] Vinesh V. Nishawala, Martin Ostoja-Starzewski, Michael J. Leamy, and Paul N. Demmie. Simulation of elastic wave propagation using cellular automata and peridynamics, and comparison with experiments. *Wave Motion*, 60:73–83, 2016.

[34] Vinesh V. Nishawala, Martin Ostoja-Starzewski, Michael J. Leamy, and Emilio Porcu. Lamb's problem on random mass density fields with fractal and Hurst effects. *Proceedings of the Royal Society of London. Series A: Mathematical and Physical Sciences*, 472(2196):20160638, 2016.

[35] Martin Ostoja-Starzewski. Random field models of heterogeneous materials. *International Journal of Solids and Structures*, 35(19):2429–2455, 1998.

[36] Martin Ostoja-Starzewski. Material spatial randomness: From statistical to representative volume element. *Probabilistic Engineering Mechanics*, 21(2):112–132, 2006.

[37] Martin Ostoja-Starzewski. Ignaczak equation of elastodynamics. *Mathematics and Mechanics of Solids*, 2018.

[38] Martin Ostoja-Starzewski, Sohan Kale, Pouyan Karimi, Anatoliy Malyarenko, Bharath Raghavan, Shivakumar I. Ranganathan, and Jun Zhang. Scaling to RVE in random media. *Advances in Applied Mechanics*, 49:111–211, 2016.

[39] Martin Ostoja-Starzewski and Jun Zhang. Does a fractal microstructure require a fractional viscoelastic model? *Fractal and Fractional*, 2(1):12, 2018.

[40] Padio-Guidugli and Antonino Favata. Elasticity for geotechnicians: a modern exposition of Kelvin, Boussinesq, Flammant, Cerrutti, Melan and Mindlin problems. *Solid Mechanics and its Applications*, 2014.

[41] Emilio Porcu. *Spatio-temporal geostatistics: new classes of covariance, variogram and spectral densities*. PhD thesis, Universitá Milano Bicocca, 2004.

[42] Emilio Porcu, Reinhard Furrer, and Douglas Nychka. 30 years of space–time covariance functions. *Wiley Interdisciplinary Reviews: Computational Statistics*, 13(2):e1512, 2021.

[43] Emilio Porcu, Jorge Mateu, Alessandro Zini, and Rita Pini. Modelling spatio-temporal data: a new variogram and covariance structure proposal. *Statistics and Probability Letters*, 77(1):83–89, 2007.

[44] Yuriy Povstenko. *Linear Fractional Diffusion-wave Equation for Scientists and Engineers.* Springer, 2015.

[45] William F. Riley and James W. Dally. A photoelastic analysis of stress wave propagation in a layered model. *Geophysics*, 31(5):881–899, 1966.

[46] Klaus Rohde. Cellular automata and ecology. *Oikos*, 110(1):203–207, 2005.

[47] Karl K. Sabelfeld and Irina Shalimova. Elastic half-plane under random displacement excitations on the boundary. *Journal of Statistical Physics*, 132(6):1071–1095, 2008.

[48] Karl K. Sabelfeld and Irina Shalimova. Elastostatics of a half-plane under random boundary excitations. *Journal of Statistical Physics*, 137(3):521, 2009.

[49] Martin Schlather. Simulation and analysis of random fields. *R News*, 1(2):18–20, 2001.

[50] Michael P. Sena, Martin Ostoja-Starzewski, and Luis Costa. Stiffness tensor random fields through upscaling of planar random materials. *Probabilistic Engineering Mechanics*, 34:131–156, 2013.

[51] Lihua Shen, Martin Ostoja-Starzewski, and Emilio Porcu. Bernoulli-Euler beams with random field properties under random field loads: fractal and Hurst effects. *Archive of Applied Mechanics*, 84(9-11):1595–1626, 2014.

[52] Lihua Shen, Martin Ostoja-Starzewski, and Emilio Porcu. Elastic rods and shear beams with random field properties under random field loads: fractal and Hurst effects. *Journal of Engineering Mechanics*, 141(7):1–8, 2015.

[53] Lihua Shen, Martin Ostoja-Starzewski, and Emilio Porcu. Harmonic oscillator driven by random processes having fractal and Hurst effects. *Acta Mechanica*, 226(11):3653, 2015.

[54] Lihua Shen, Martin Ostoja-Starzewski, and Emilio Porcu. Responses of first-order dynamical systems to Matérn, Cauchy, and Dagum excitations. *Mathematics and Mechanics of Complex Systems*, 3(1):27–41, 2015.

[55] Christian Soize. Identification of high-dimension polynomial chaos expansions with random coefficients for non-gaussian tensor-valued random fields using partial and limited experimental data. *Computer Methods in Applied Mechanics and Engineering*, 199(33-36):2150–2164, 2010.

[56] Thomas Chi Tsai Ting. *Anisotropic Elasticity: Theory and Applications.* Number 45. Oxford University Press on Demand, 1996.

[57] Jean Virieux. SH-wave propagation in heterogeneous media: velocity-stress finite-difference method. *Geophysics*, 49(11):1933–1942, 1984.

[58] John von Neumann. Theory of self-reproducing automata. *IEEE Transactions on Neural Networks and Learning Systems*, 5(1):3–14, 1966.

[59] Stephen Wolfram. Statistical mechanics of cellular automata. *Reviews of Modern Physics*, 55(3):601, 1983.

[60] Stephen Wolfram. Computation theory of cellular automata. *Communications in Mathematical Physics*, 96(1):15–57, 1984.

[61] Stephen Wolfram. Universality and complexity in cellular automata. *Physica D: Nonlinear Phenomena*, 10(1-2):1–35, 1984.

[62] Robert L. Wolpert and Katja Ickstadt. Poisson/Gamma random field models for spatial statistics. *Biometrika*, 85(2):251–267, 1998.

[63] Xian Zhang, Anatoliy Malyarenko, Emilio Porcu, and Martin Ostoja-Starzewski. Elastodynamic problem on tensor random fields with fractal and Hurst effects. *Meccanica*, 2021 (in press).

[64] Xian Zhang, Vinesh V. Nishawala, and Martin Ostoja-Starzewski. Anti-plane shear Lamb's problem on random mass density fields with fractal and Hurst effects. *Evolution Equations and Control Theory*, 8(1):231–246, 2019.

[65] Xian Zhang and Martin Ostoja-Starzewski. Impact force and moment problems on random mass density fields with fractal and Hurst effects. *Philosophical Transactions of the Royal Society A*, 378(2172):20190591, 2020.